Superconducting Microresonators: Physics and Applications

Jonas Zmuidzinas

Division of Physics, Mathematics, and Astronomy, California Institute of Technology, Pasadena, California 91125; email: jonas@submm.caltech.edu

Annu. Rev. Condens. Matter Phys. 2012. 3:169–214

The *Annual Review of Condensed Matter Physics* is online at conmatphys.annualreviews.org

This article's doi: 10.1146/annurev-conmatphys-020911-125022

1947-5454/12/0310-0169$20.00

Keywords

detectors, kinetic inductance, microwave, quantum, superconductivity

Abstract

Interest in superconducting microresonators has grown dramatically over the past decade. Resonator performance has improved substantially through the use of improved geometries and materials as well as a better understanding of the underlying physics. These advances have led to the adoption of superconducting microresonators in a large number of low-temperature experiments and applications. This review outlines these developments, with particular attention given to the use of superconducting microresonators as detectors.

1. INTRODUCTION

Superconducting microresonators are simple and versatile devices. Although superconducting microresonators have been used since the 1960s, interest in these devices has grown especially rapidly over the past decade, triggered by the demonstration of high-performance transmission-line microresonators as sensitive photon detectors (1) and the subsequent adoption of this type of resonator for quantum-state readout of superconducting qubits (2). Superconducting microresonators are now the subject of intense study and are targeted for a wide variety of applications including dark matter search experiments, neutrino mass experiments, frequency-multiplexed readout of cryogenic detector arrays, quantum circuits including qubit readout, simulation of quantum many-body systems, coupling to nanomechanical systems, and quantum-limited parametric amplifiers. Combined, these applications exploit a broad range of phenomena in superconductivity, including ultralow dissipation, the kinetic inductance effect, nonlinear response, and nonequilibrium dynamics. The relative ease of probing these phenomena in a wide range of materials using microresonator measurements has stimulated a fresh look at these topics and has led to significant advances in several areas. In addition, understanding the detailed behavior of superconducting microresonators requires branching out into other areas of condensed matter physics, especially two-level systems (TLS) in amorphous materials.

In the simplest case, a superconducting microresonator may be produced by depositing a superconducting thin film on an insulating substrate and applying standard lithographic patterning techniques to produce a resonator structure. As illustrated in **Figure 1**, the resonator may either be a lumped-element circuit, e.g., a meandered inductor and an interdigitated capacitor, or a transmission-line resonator. These simple single-layer structures permit use of high-quality crystalline substrates and a wide variety of superconducting films, and therefore provide an opportunity to achieve extremely low dissipation. Indeed, much recent research has focused on understanding the physical origin of the remaining dissipation and finding ways to reduce it.

In this review, I focus on the observed properties of superconducting microresonators, the interpretation of the results using physical models, and the behavior of these devices when used as photon detectors before concluding with a survey of other microresonator applications. To set the stage, I start with a brief review of the basics of superconductor electrodynamics and its historical development. This is followed by a short summary of the results obtained with standard superconducting cavity resonators, providing a transition from electrodynamics to microresonators.

Microresonators are very attractive for detector applications because of their simplicity and because large arrays can be read out using frequency-domain multiplexing. Due to space limitations, little will be said about the science drivers that motivate the detector applications, nor will any attempt be made to place superconducting microresonator detectors in context; other sources can be consulted to fill in these gaps. A more general review describing the status and applications of millimeter-wave through far-IR superconducting detectors was given by Zmuidzinas & Richards (3); Moseley (4) provides an updated view. Mazin (5) discusses the history and applications of superconducting microresonator detectors. Irwin & Hilton (6) give a detailed review of the physics and applications of a different type of superconducting detector, the transition edge sensor. For additional information on detectors and applications, the proceedings of the biannual Low Temperature Detectors conference (7) are a good place to start.

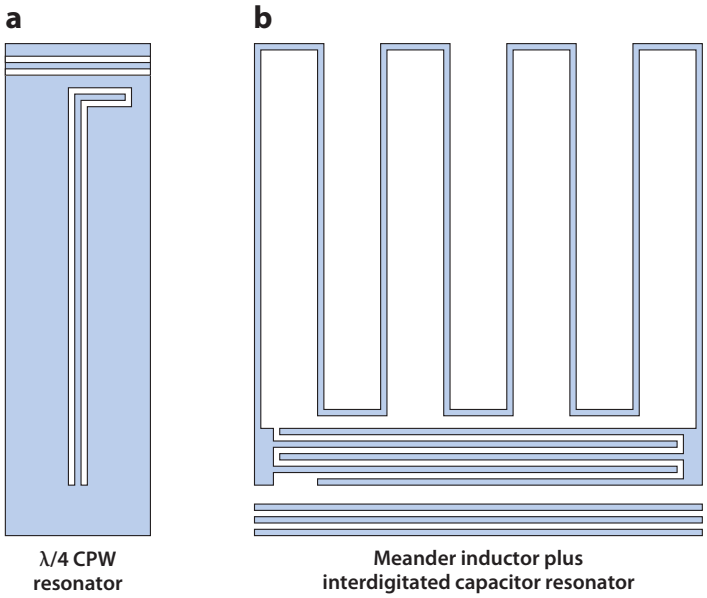

Figure 1

This figure illustrates two simple microresonator geometries that may be fabricated by patterning a superconducting film. Blue shaded regions represent areas covered by the superconducting film; white regions represent areas where the film has been etched away to reveal the bare substrate. (*a*) A λ/4 coplanar-waveguide (CPW) shunt-coupled transmission line resonator. The CPW feedline used to excite the resonator is visible at the top. (*b*) A lumped-element resonator consisting of a meandered inductor and an interdigitated capacitor. The CPW feedline visible at the bottom has finite-width ground strips and couples to the interdigitated capacitor.

2. SUPERCONDUCTOR ELECTRODYNAMICS

2.1. Historical Background

Heike Kamerlingh Onnes's 1911 discovery (8) illustrated the most familiar hallmark of superconductivity: the vanishing of the electrical resistance below the transition temperature T_c. Two decades later, experiments (9, 10) showed that a large change in conductivity at the transition could be seen not only using direct currents, but also using alternating radio-frequency (RF; 1–10 MHz) currents. By 1940 (11), this behavior was observed at microwave frequencies (1.5 GHz). It became clear that the electrical conductivity $\sigma(\omega)$ must exhibit a change from superconducting behavior to normal metal behavior at frequencies ω between the microwave and IR bands, because no significant change in the optical absorption was observed upon passing through the superconducting transition (12). This behavior was soon exploited to make the first superconducting IR bolometers (13). The crossover from superconducting to normal behavior was eventually shown to occur in the millimeter through far-IR wavelength range (14, 15, 16), consistent with a temperature-dependent electron energy gap of $2\Delta(T)$ (with $2\Delta \approx 3.5\ kT_c$ for $T << T_c$), which was a key feature of the Bardeen-Cooper-Schrieffer (BCS) theory published shortly thereafter (17, 18).

Several decades before the electron-pairing BCS theory was proposed, Heinz London predicted (19) that a superconductor should in general have a small but nonzero dissipation for AC currents. This stands in contrast to the DC case, for which the resistance and associated

dissipation vanish entirely for $T < T_c$, as illustrated by the Meissner effect. The dissipation arises because the finite inertia of the superconducting electrons allows AC electric fields to exist inside a superconductor, and therefore the presence of a small fraction of normal electrons, as expected for temperatures above absolute zero, leads to, in London's words, "production of heat."

2.2. The Mattis-Bardeen Theory

The application of the BCS theory to the calculation of the electrical conductivity of superconductors yielded results consistent with London's insight. Indeed, for frequencies below the gap frequency, $\omega_g/2\pi = \nu_g = 2\Delta/h \approx 74\ \text{GHz} \times (T_c/1\ \text{K})$, the Mattis-Bardeen equations (20) for the complex conductivity $\sigma(\omega) = \sigma_1(\omega) - i\sigma_2(\omega)$ relative to the normal-state conductivity $\sigma_n = 1/\rho_n$ read as

$$\frac{\sigma_1(\omega)}{\sigma_n} = \frac{2}{\hbar\omega}\int_{\Delta}^{\infty} dE \frac{E^2 + \Delta^2 + \hbar\omega E}{\sqrt{E^2 - \Delta^2}\sqrt{(E+\hbar\omega)^2 - \Delta^2}}[f(E) - f(E+\hbar\omega)] \quad 1.$$

and

$$\frac{\sigma_2(\omega)}{\sigma_n} = \frac{1}{\hbar\omega}\int_{\Delta}^{\Delta+\hbar\omega} dE \frac{E^2 + \Delta^2 - \hbar\omega E}{\sqrt{E^2 - \Delta^2}\sqrt{\Delta^2 - (E-\hbar\omega)^2}}[1 - 2f(E)]. \quad 2.$$

The complex conductivity is a valid concept provided that a local version of Ohm's law applies, $\vec{J}(\vec{r}) = \sigma(\omega)\vec{E}(\vec{r})$. This local limit is often of practical interest, and occurs when the electron mean free path is short compared to the depth to which the field penetrates below the surface of the superconductor. The quantity $f(E)$ is the distribution function for unpaired normal electrons or quasiparticles (21), and in the case of thermal equilibrium is given by the Fermi-Dirac distribution $f(E) = 1/(e^{E/kT}+1)$. The corresponding quasiparticle density is given by the equation

$$n_{qp} = 4N_0\int_{\Delta}^{\infty} dE \frac{E}{\sqrt{E^2 - \Delta^2}} f(E), \quad 3.$$

where N_0 is the single-spin density of electron states at the Fermi energy. The quasiparticles suppress the gap Δ relative to the zero-temperature value Δ_0 according to

$$\frac{\Delta_0 - \Delta}{\Delta_0} \approx -\ln\left(\frac{\Delta}{\Delta_0}\right) = 2\int_{\Delta}^{\infty} dE \frac{1}{\sqrt{E^2 - \Delta^2}} f(E), \quad 4.$$

which illustrates that quasiparticles closest to the gap are most effective because the weighting varies as $1/E$. At low temperatures, $T << T_c$, $f(E \geq \Delta)$ decreases exponentially, varying as $e^{-E/kT} \leq e^{-\Delta/kT}$. Therefore, as $T \to 0$, $\Delta - \Delta_0$, n_{qp}, σ_1 all vanish exponentially as $e^{-\Delta/kT}$, because these quantities are linearly proportional to $f(E)$. Thus, in theory the microwave dissipation of a superconductor may be made arbitrarily low—one simply needs to operate at a sufficiently low temperature. However, the imaginary part of the conductivity, associated with the inertia of the superconducting electrons, remains finite:

$$\frac{\sigma_2(\omega, 0)}{\sigma_n} = \frac{\pi\Delta_0}{\hbar\omega}\left[1 - \frac{1}{16}\left(\frac{\hbar\omega}{\Delta_0}\right)^2 - \frac{3}{1024}\left(\frac{\hbar\omega}{\Delta_0}\right)^4 + \ldots\right]. \quad 5.$$

Note that the leading $1/\omega$ factor reflects the finite inertia of the Cooper pairs. These behaviors indicate that at low temperatures, i.e., $T << T_c$, the dissipative response of the

electron system is very small compared to the reactive response, $\sigma_1 << \sigma_2$, reflecting the relative paucity of quasiparticles compared to Cooper pairs. If we look more closely, we find that $\delta\sigma_2(\omega, T) = \sigma_2(\omega, T) - \sigma_2(\omega, 0) \propto e^{-\Delta/kT}$ because this quantity is also linearly proportional to $f(E)$. Thus, both σ_1 and $\delta\sigma_2$ are proportional to the quasiparticle density n_{qp} for $T << T_c$.

2.3. Surface Impedance

In most cases, the complex conductivity is not directly accessible experimentally; instead, the complex surface impedance $Z_s = R_s + iX_s$ is the quantity being probed. Calculation of the surface impedance in the general case is not simple and requires numerical techniques; References 22–24 provide entry points into the literature and should be consulted for more detail. However, examination of several simple limiting cases provides considerable insight. For thick films in the local limit, the surface impedance and complex conductivity are related by

$$Z_s(\omega, T) = \sqrt{\frac{i\mu_0\omega}{\sigma(\omega, T)}} = \frac{Z_s(\omega, 0)}{\sqrt{1 + i\delta\sigma(\omega, T)/\sigma_2(\omega, 0)}}, \quad 6.$$

where $\delta\sigma(\omega, T) = \sigma(\omega, T) - \sigma(\omega, 0) = \sigma_1(\omega, T) - i\delta\sigma_2(\omega, T)$. The theoretical surface impedance at zero temperature is purely reactive and may be expressed in terms of the penetration depth λ:

$$Z_s(\omega, 0) = i\mu_0\omega\lambda, \quad 7.$$

where, in the local limit,

$$\lambda_{\text{local}} = \sqrt{\frac{\hbar}{\pi\Delta\mu_0\sigma_n}} \approx 105\text{nm} \times \sqrt{\frac{\rho_n}{1\mu\Omega\text{cm}}\frac{1\text{K}}{T_c}}. \quad 8.$$

A similar equation may be written for thick films in the extreme anomalous regime, which occurs when the response is no longer local because the electron mean free path l is long compared to the distance over which the field varies significantly:

$$Z_s(\omega, T) = i\mu_0\omega\lambda[1 + i\delta\sigma(\omega, T)/\sigma_2(\omega, 0)]^{-1/3}, \quad 9.$$

where the complex conductivity is still calculated according to Equations 1 and 2, except that now the penetration depth is given by

$$\lambda_{\text{e.a.}} = \lambda_{\text{local}}\left[\frac{\sqrt{3}l}{2\pi\lambda_{\text{local}}}\right]^{1/3}, \quad 10.$$

and is in fact independent of l because $\lambda_{\text{local}} \propto l^{-1/2}$. Equations 6 and 9 hold when the superconductor is thick compared to the corresponding penetration depth, $t >> \lambda$. If the opposite is true and we are dealing with superconducting films that are sufficiently thin so that the current density is essentially constant throughout the film thickness t, we may write

$$Z_s(\omega, T) = i\mu_0\omega\lambda[1 + i\delta\sigma(\omega, T)/\sigma_2(\omega, 0)]^{-1}, \quad 11.$$

if, in this expression, we use an effective penetration depth for thin films,

$$\lambda_{\text{thin}} = \frac{\lambda_{\text{local}}^2}{t}. \quad 12.$$

For a film that is thin enough so that diffusive surface scattering limits the electron mean free path, Equation 8 gives $\lambda^2_{\rm local} \propto \rho_n \propto 1/t$, and the effective penetration depth varies inversely as the square of the film thickness, $\lambda_{\rm thin} \propto 1/t^2$.

These results may be summarized by relating the first-order fractional perturbation in the surface impedance to the fractional perturbation in the conductivity,

$$\frac{\delta Z_s(\omega, T)}{Z_s(\omega, 0)} \approx -\gamma \frac{\delta\sigma(\omega, T)}{\sigma(\omega, 0)}, \qquad 13.$$

where $\delta Z_s(\omega, T) = Z_s(\omega, T) - Z_s(\omega, 0)$, and with $\gamma = 1$, 1/2, and 1/3 for the thin-film, local, and extreme anomalous limits, respectively. We introduce the conductivity quality factor,

$$Q_\sigma(\omega, T) = \frac{\sigma_2(\omega, T)}{\sigma_1(\omega, T)}, \qquad 14.$$

and similarly the surface impedance quality factor,

$$Q_s = \frac{X_s(\omega, T)}{R_s(\omega, T)}. \qquad 15.$$

For $Q_\sigma >> 1$, we may approximate $Q_\sigma(\omega, T) \approx \sigma_2(\omega, 0)/\sigma_1(\omega, T)$ to a fractional accuracy of order Q_σ^{-1}. Equation 13 may then be used to show $Q_s = Q_\sigma/\gamma$.

Figure 2 shows a plot of Q_σ as predicted by the Mattis-Bardeen theory. At low frequencies and temperatures, $\hbar\omega << \Delta_0$ and $k_B T << \Delta_0$, we may use the approximation (25)

$$\frac{\sigma_1}{\sigma_n} \approx \frac{4\Delta}{\hbar\omega} e^{-\Delta_0/k_B T} \sinh\left(\frac{\hbar\omega}{2k_B T}\right) K_0\left(\frac{\hbar\omega}{2k_B T}\right), \qquad 16.$$

along with Equation 5, to obtain

$$Q_\sigma(\omega, T) \approx \frac{\pi}{4} \frac{e^{\Delta_0/k_B T}}{\sinh(\hbar\omega/2k_B T)\, K_0\,(\hbar\omega/2k_B T)}, \qquad 17.$$

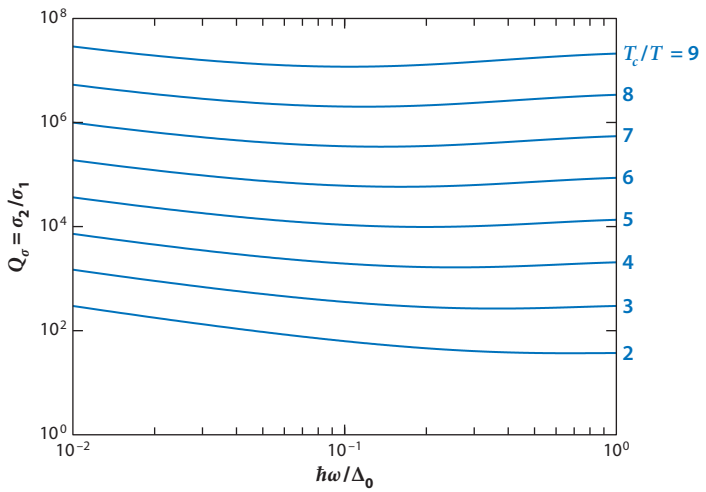

Figure 2

A plot of the complex conductivity quality factor $Q_\sigma = \sigma_2/\sigma_1$ as a function of normalized frequency $\hbar\omega/\Delta_0$, calculated using the Mattis-Bardeen integrals (Equations 1 and 2). Note that the minimum occurs roughly at $\hbar\omega/\Delta_0 \sim T/T_c$. At low frequencies, $Q_\sigma \propto 1/\omega$ as indicated by Equation 18.

which explicitly shows the exponential rise with decreasing temperature [note $\sinh(x)$ $K_0(x) \sim \sqrt{\pi/8x}$ as $x \to \infty$]. In the limit $\hbar\omega << k_B T$, this result may be further approximated as

$$Q_\sigma(\omega, T) \approx \frac{\pi}{2} \frac{e^{\Delta_0/k_B T}}{[\ln(4k_B T/\hbar\omega) - \gamma_{\rm EM}]} \frac{k_B T}{\hbar\omega}, \qquad 18.$$

illustrating the $1/\omega$ dependence at low frequencies visible in **Figure 2**. Here $\gamma_{\rm EM} = 0.577\ldots$ is the Euler-Mascheroni constant.

2.4. Density of States Broadening

Another issue to consider, especially for high-resisitivity materials such as TiN or NbTiN, is the possibility that the density of states function $\rho(E)$ is broadened relative to that predicted by the BCS theory. Indeed, on the basis of tunneling spectra measured for granular aluminum films at temperatures $T << T_c$, Dynes et al. (26) argue that the density of states is well approximated by the form

$$\rho(E, \Gamma) = {\rm Re}\left\{ \frac{E - i\Gamma}{[(E - i\Gamma)^2 - \Delta^2]^{1/2}} \right\}, \qquad 19.$$

which results from making the substitution $E \to E - i\Gamma$ into the BCS density of states function. Here, Γ is the energy broadening parameter; Dynes et al. found a roughly linear dependence between the resistivity and the best-fit value of Γ. The effect of energy broadening on the surface impedance can be calculated by substituting the broadened density of states into the Mattis-Bardeen equations (1, 2). This approach has been followed by Barends et al. (27) in their analysis of a NbTiN coplanar waveguide (CPW) resonator, and has also been discussed by Noguchi et al. (28). Note that Mitrović & Rozema (29) argue that the correct form for the broadened density of states is obtained by providing the gap parameter with an imaginary part, $\Delta \to \Delta - i\Gamma$, rather than the energy. Furthermore, while disorder may smear the singularity near the gap, the density of states in the sub-gap region of a disordered superconductor is theoretically expected to decay very rapidly, as an exponential rather than as a Lorentzian (30; as emphasized by M. Skvortsov). A careful experimental study of the properties of high-Q microresonators over a broad range of frequency and temperature could further illuminate this issue. Finally, as a note of caution when interpreting tunneling data, Pekola et al. (31) have shown that thermal noise from the environment can produce photon-assisted tunneling currents in normal-insulator-normal (NIS) tunnel junctions that mimic the effect of a broadened density of states.

3. SUPERCONDUCTING CAVITY RESONATORS

The tremendous technical advances resulting from the development of radar in World War II revitalized the study of microwave superconductivity (32–34). Superconducting microwave cavity resonators quickly became the focus of many of these experiments because the high quality factors that could be achieved allowed subtle details of the electrodynamics to be measured. Furthermore, high-quality cavities were needed for applications, especially for use in particle accelerators. These studies showed that, in contrast to the remarkable Mattis-Bardeen prediction, the microwave dissipation did not continue its exponential decrease indefinitely as the temperature was reduced to values far below T_c. Instead, the surface resistance approached a nonzero limiting or residual value, $R_{\rm res}$, whose value was not

intrinsic to the superconductor (often niobium) but instead dependent on the quality and production methods of the materials used; cavity fabrication and assembly procedures; surface conditions including oxidation, polishing methods, and protective coatings; heat treatments, bake-out and cooldown protocols; magnetic shielding and flux trapping, etc. With sufficient attention to these details, remarkably high resonator quality factors were achieved, of order $Q_r \sim 10^{11}$ or higher (35–41).

In general, a freely oscillating cavity or resonator will lose energy due to dissipative losses as well as due to the coupling to the external circuit. The external circuit is usually a transmission line or waveguide (or several of these) capable of carrying away power to a remote termination, and therefore has a dissipative impedance. The overall resonator quality factor Q_r is given by

$$\frac{1}{Q_r} = \frac{1}{Q_i} + \frac{1}{Q_c}, \qquad 20.$$

where the internal quality factor Q_i describes the dissipative losses and the coupling quality factor Q_c describes the strength of the coupling. For a cavity, the internal and surface impedance quality factors, Q_i and Q_s, are related by a coefficient that characterizes the fraction of the cavity energy that is stored in the penetration-depth layer. This fraction is quite small, so $Q_i >> Q_s$:

$$Q_i = gQ_s \frac{\lambda_{\mathrm{RF}}}{\lambda_{\mathrm{sc}}}, \qquad 21.$$

where g is a geometrical factor of order unity (typically ~ 0.3) dependent on the cavity geometry and mode, $\lambda_{\mathrm{RF}} = c/\nu$ is the free-space wavelength, and $\lambda_{\mathrm{sc}} << \lambda_{\mathrm{RF}}$ is the field penetration depth of the superconductor. The maximum surface impedance quality factor achieved with niobium cavities in the 1.5 – 22 GHz frequency range is $Q_s = X_s/R_{\mathrm{res}} \sim 2 \times 10^5$ (35, 39, 41).

4. SUPERCONDUCTING MICRORESONATORS

4.1. Thin-Film Transmission Lines

Pippard (33) understood that the use of a superconductor in a parallel-strip transmission line, similar to what is today known as a microstrip line (see **Figure 3**), would result in a change of the phase velocity due to the inductance contributed by the surface impedance, $Z_s(\omega, 0) = iX_s = i\omega L_s = i\omega\mu_0\lambda_{\mathrm{sc}}$. Indeed, the inductance per unit length of a line made using a perfect conductor ($\sigma \to \infty$) is approximately given by $\mathcal{L} = \mu_0 h/w$, where h is the dielectric thickness and w is the microstrip width, provided that $w >> h$ so that fringing fields may be ignored. The capacitance per unit length in this limit is $\mathcal{C} = \epsilon_r\epsilon_0 w/h$, where ϵ_r is the relative dielectric constant of the substrate. The phase velocity of the fundamental TEM-like mode is $\bar{c} = 1/\sqrt{\mathcal{L}\mathcal{C}} = c/\sqrt{\epsilon_r}$. As discussed by Pippard and others (33, 42–45), the use of a superconductor causes an increase in the inductance, $\mathcal{L} = \mu_0(h + 2\lambda_{\mathrm{sc}})/w$, as if the spacing between the superconducting films had increased by $2\lambda_{\mathrm{sc}}$. The capacitance remains unchanged because the scale length for screening of electric fields in a conductor is of atomic scale. The fraction of the total inductance of the line that is contributed by the superconductor is

$$\alpha_{\mathrm{ms}} = \frac{2\lambda_{\mathrm{sc}}}{h + 2\lambda_{\mathrm{sc}}}. \qquad 22.$$

The increased inductance causes a reduction in the phase velocity, by the factor $\sqrt{1 - \alpha_{\mathrm{ms}}}$, to $\bar{c} = (1 + 2\lambda_{\mathrm{sc}}/h)^{-1/2} c/\sqrt{\epsilon_r}$. More accurate expressions for the properties of superconducting

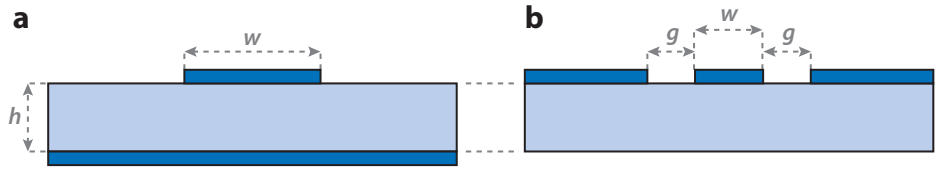

Figure 3

This figure shows cross sections of two planar transmission-line structures. Dark blue regions represent superconducting films; the light blue regions represent the dielectric. (*a*) A microstrip transmission line consists of a conducting strip of width w on the surface of a dielectric slab of thickness h backed by a conducting ground plane. This layer structure may be free standing or may reside on top of a thicker substrate. The coplanar-waveguide line, illustrated in panel *b*, has conductors only on the top surface of the dielectric and consists of a center strip of width w separated from ground planes on either side by gaps of width g.

microstrip lines that include the effects of fringing fields may be found in the literature (46, 47). Alternatively, microstrip properties may be quickly calculated using modern electromagnetic simulation software.

Microstrip lines may be fabricated by depositing three film layers (superconductor, insulator, superconductor) on a substrate and patterning the top superconductor layer. In this case, the dielectric thickness h would typically lie in the range of 0.1 – 1 μm. Alternatively, the substrate may itself serve as the microstrip dielectric, with superconducting films deposited on the top and bottom surfaces, in which case $h \sim 100 - 500$ μm. In both cases, h is quite small compared to the free-space wavelength $\lambda_{RF} \approx 30$ cm $\times$ (1 GHz/ν), so $\alpha_{ms} >> \lambda_{sc}/\lambda_{RF}$. Therefore, compared to a cavity resonator (Equation 21), a microstrip resonator limited by conductor losses has a considerably lower internal quality factor $Q_i = \alpha_{ms}^{-1} Q_s$ for the same value of Q_s. As Pond et al. (45) point out, the kinetic inductance fraction can even approach unity if a thin superconducting film with a high normal-state resistivity ρ_n is used (see Equations 8 and 12). For some applications, e.g., low-noise oscillators, the lower quality factor of microresonators as compared to cavity resonators is a serious disadvantage. For other applications, e.g., detectors, the combination of high kinetic inductance fraction and very small active volume provides microresonators with a tremendous advantage.

The CPW (**Figure 3**) is another popular superconducting transmission line structure. One advantage of CPW as compared to microstrip is that only one superconducting film layer is required. However, the kinetic inductance fraction of CPW is generally smaller than that for thin-film microstrip. This can be seen from the crude estimate $\alpha_{CPW} \sim \lambda_{sc}/w$, and by noting that typical CPW center strip widths $w \sim 2 - 10$ μm are larger than the 0.1 – 1 μm film thickness of deposited dielectrics used for microstrip lines. The kinetic inductance fraction of superconducting CPW lines may be accurately calculated using analytical formulae (48), conformal mapping methods (24), or direct electromagnetic simulation, and these methods generally yield results consistent with measurements (49).

4.2. A Brief History

It has long been appreciated that superconducting thin-film transmission lines and resonators could be very useful in a number of applications; however, success in these applications depends on the level of resonator performance that can be achieved in practice. For example, although Landauer (50) patented a concept in 1963 for a superconducting kinetic inductance parametric amplifier using thin-film resonators, a kinetic inductance parametric amplifier has only recently

been demonstrated (51). As we outline below, microresonator performance has been improving steadily since the 1960s, with an especially rapid increase over the past decade. This progress can be attributed to the use of better materials, improved fabrication tools and processes, attention to experimental conditions such as shielding of magnetic fields and stray radiation (52), and, especially, a better understanding of the relevant physics.

In 1969, Mason & Gould published a study (43) of In/Ta_2O_5/Ta microstrip resonators in the 50–500 MHz range. The microstrips were made using evaporated thin In films on anodized Ta substrates. The highest resonator quality factors achieved were $Q_r \sim 1.7{\times}10^3$. Mason & Gould's results showed that a surface impedance quality factor of at least $Q_s \geq \alpha_{ms} Q_r \sim 8 \times 10^2$ was possible, a limit that was two orders of magnitude lower than contemporary cavity measurements. DiNardo et al. (53) obtained much higher quality factors, around $Q_r = 5 \times 10^5$ at 14 GHz, using thin-film lead microstrips on alumina substrates. However, the relatively thick substrates used yield low values of α_{ms}, so the inferred value of $Q_s \sim 5 \times 10^2$ is actually similar to the limit set by Mason & Gould.

About a decade later, Pöpel (54) studied the losses of PbAu/SiO/Pb microstrip resonators, finding minimum losses at $T = 1.7$ K of 0.04 dB/m at 9.1 GHz and 0.09 dB/m at 27.3 GHz, respectively, corresponding to quality factors of $\sim 6 \times 10^4$. Given the 880-nm thickness of the SiO dielectric, the kinetic inductance fraction was around $\alpha_{ms} \approx 0.12$, so a value of $Q_s \sim 7 \times 10^3$ was achieved, a significant step forward and not far from the Mattis-Bardeen value at $T_c/T = 4.2$ (see **Figure 2**). Pond et al. (45) studied NbN/Si:H/NbN microstrip resonators in the 0–2 GHz frequency range. Using magnetron sputtering, rather thin films (150 Å, 400 Å, 140 Å) were deposited, and the measured phase velocity $\bar{c}/c = 0.016$ was very low, indicating a kinetic inductance fraction close to unity, as would be expected. The line loss was also measured and indictated $Q_s \sim 3 - 6 \times 10^3$. In 1993, Andreone et al. (55) reported results from microstrip resonators made by depositing and patterning both Nb ($\rho_n = 2.6$ $\mu\Omega$ cm) and NbTiN ($\rho_n =$ 90 $\mu\Omega$ cm) films on sapphire substrates. The resonator was formed by inverting the substrate and placing it on top of another sapphire substrate, with a bulk niobium foil below serving as the ground plane. The kinetic inductance fraction of this arrangement is quite low due to the 130-μm substrate thickness. The measurement fits indicate zero-temperature residual surface resistances of 1.3 $\mu\Omega$ (Nb) and 5.9 $\mu\Omega$ (NbTiN), which correspond to $Q_s \approx 1.3 \times 10^3$ for both films, which is comparable to or somewhat lower than earlier work.

Starting in 2000, the possibility of using superconducting microresonators as detectors stimulated exploratory measurements at Caltech and the Jet Propulsion Laboratory (JPL). Initially this work was focused on thin-film microstrip resonators. Using materials such as Nb and Al and with evaporated SiO as the dielectric, resonator quality factors around 5×10^4 were measured (see **Figure 4**). However, these resonators showed complex behavior as a function of temperature and microwave power that deviated strongly from the Mattis-Bardeen predictions. This behavior was not understood at the time; in 2005 the work of Martinis et al. (56) showed that TLS in the amorphous thin-film dielectric were likely responsible for these effects. Considerably better microstrip resonators have since been demonstrated (57).

In an effort to simplify the situation, the Caltech/JPL group switched to resonators using CPW lines (see **Figures 1**, **3,** and **5**), made from a single superconducting film deposited on a high-quality crystalline substrate such as silicon or sapphire. In some cases, very high-quality factors were achieved, around $Q_r = 2 \times 10^6$ (1, 58), indicating a surface impedance quality factor of at least $Q_s \sim 10^5$. These results have now been reproduced and extended by a number of other groups (59, 60).

In 2008, Barends et al. (27) published measurements of a CPW resonator made using NbTiN deposited on a silicon substrate. The 300-nm-thick NbTiN film with $T_c = 14.8$ K had a

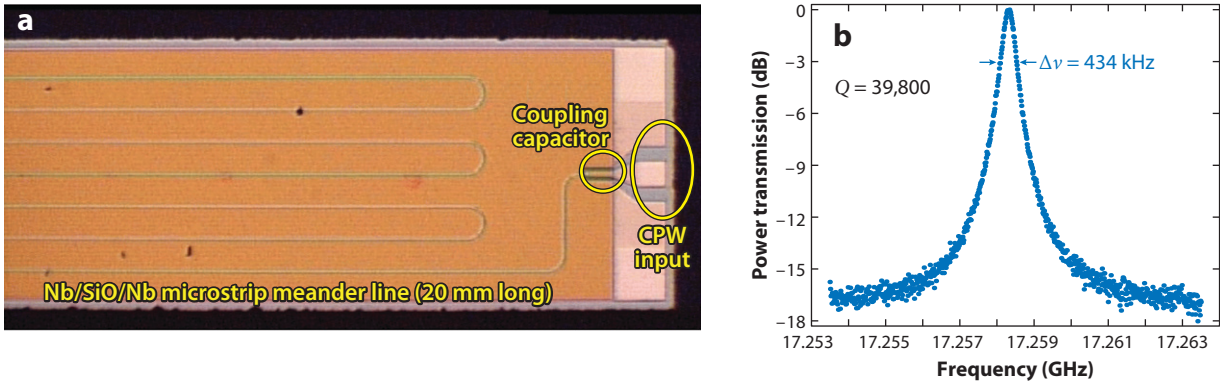

Figure 4

(*a*) Photograph of a half-wave Nb/SiO/Nb microstrip resonator measured at Caltech/JPL in February 2000. The coupling capacitor is a parallel-plate Nb/SiO/Nb structure. (*b*) Measurement results at 17.26 GHz with relatively high microwave power, showing $Q_r = 4 \times 10^4$. This resonance is the sixth harmonic of the 2.86-GHz fundamental resonance. Credit: A. Vayonakis & H.G. Leduc. Abbreviation: CPW, coplanar-waveguide.

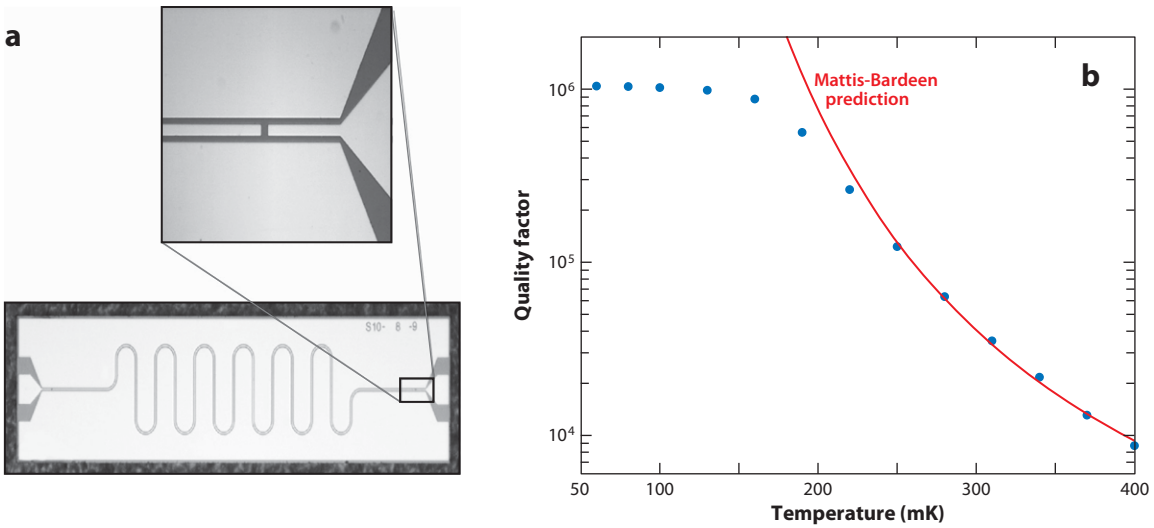

Figure 5

(*a*) Photograph of a Caltech/JPL half-wave coplanar-waveguide resonator made using an aluminum film deposited on a sapphire substrate. (*b*) Measurements obtained in early 2002 of the quality factor versus temperature, showing $Q_r = 10^6$. The curve shows the Mattis-Bardeen prediction. Credit: P.K. Day, B.A. Mazin & H.G. Leduc.

resistivity of $\rho_n = 170\ \mu\Omega$ cm, which was several orders of magnitude higher than standard metals, giving a large kinetic inductance fraction of $\alpha_{CPW} = 0.35$. The measured quality factor was $Q_r = 6 \times 10^5$, indicating a lower limit to the surface impedance quality factor of $Q_s = 3 \times 10^5$. This result was surprisingly high, over two orders of magnitude improvement compared to the measurements of Andreone et al. (55), and comparable to or even somewhat better than the results for niobium cavities and aluminum CPW resonators. Even higher values of Q_s were established in 2010 by Leduc et al. (61) using TiN films patterned into

lumped-element resonators (62) of the type shown in **Figure 1**. Stoichiometric TiN films deposited on silicon substrates gave $T_c = 4.5$ K, $\rho_n = 100$ $\mu\Omega$ cm, and a kinetic inductance fraction $\alpha = 0.74$. The measured internal quality factor $Q_i = 3 \times 10^7$ indicates a lower limit of $Q_s = 2 \times 10^7$. TiN resonators with high internal quality factors have now been reproduced in other laboratories (60, 63).

4.3. Radiation Loss

As illustrated in **Figure 6**, the performance of superconducting microresonators has improved dramatically over the past four decades. Resonator quality factors above 10^6 are now routinely achieved using single-layer structures deposited on high-quality, low-loss crystalline substrates. Achieving high-quality factors requires minimizing all potential sources of dissipation including loss due to radiation into free space. Loss due to radiation into the external circuit is accounted for by the coupling quality factor Q_c and may be engineered by varying the proximity of the resonator to the readout feedline. Incidentally, using a large value of Q_c strongly suppresses photon thermal conduction between the resonator and the readout circuit (64). As a general rule, free-space radiation loss may be minimized by allowing currents with opposite polarities to flow in close proximity. As a result, any radiation produced by current in one polarity is very nearly cancelled by the radiation from the opposite polarity. Low radiation loss at microwave frequencies is therefore readily achievable using the small, micron-scale feature sizes available with modern lithography. A rough estimate of radiation loss may be made by considering a 50-Ω, half-wave CPW resonator on a semi-infinite substrate with dielectric constant $\varepsilon_r = 10$.

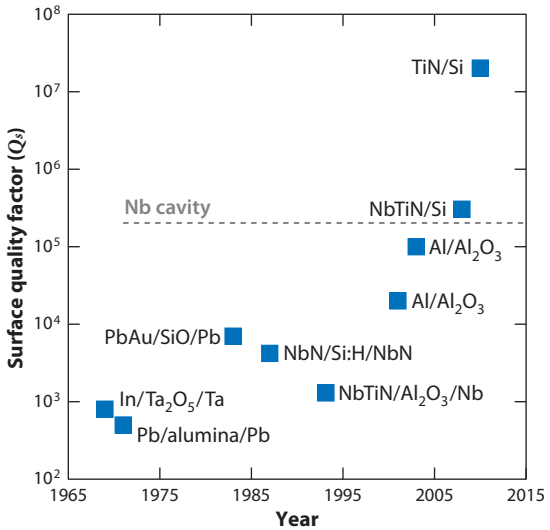

Figure 6

This plot shows lower limits to the surface impedance quality factor Q_s derived from measurements of superconducting microresonators. The lower limits are derived by assigning the total measured resonator loss to the superconductor. Points labeled by three materials are microstrip structures. Points labeled by two materials indicate resonators made from a single superconducting film deposited on a crystalline substrate. The gray dashed line indicates typical results achieved with bulk Nb cavities, as discussed in Section 3. The blue points plotted are limited to the work discussed in Section 4 and do not represent a comprehensive literature search. Nonetheless, the graph serves to illustrate the general trend.

The electric field distribution in the CPW slots follows a sinusoidal standing-wave shape to high accuracy, so techniques developed to calculate the fields radiated by slot antennas (65, 66) may be applied. If the kinetic inductance fraction is small so that the effect on the phase velocity may be neglected, this structure has a radiation quality factor (A. Vayonakis & J. Zmuidzinas, unpublished calculation; 67) of

$$Q_{\mathrm{rad}} \approx 5 \times 10^{-3} \left(\frac{\lambda_0}{w}\right)^2. \qquad 23.$$

Here λ_0 is the free-space wavelength at the resonance frequency and w is the center strip width. For $Q_{\mathrm{rad}} > 10^6$, we require $w/\lambda_0 < 7 \times 10^{-5}$, or $w < 2$ μm at 10 GHz. Radiation loss may be reduced by using lower frequencies, minimizing the size of the resonator structure through the use of high kinetic inductance materials such as TiN or NbTiN, adopting a lumped-element resonator design as shown in **Figure 1**, or all of the above.

4.4. Dissipation from Two-Level Systems

In practice, the maximum internal quality factor Q_i of superconducting microresonators is often not limited by the superconducting material or radiation but instead by dissipation due to TLS in amorphous dielectrics. Such material is clearly present in the case that the resonator capacitor is a parallel-plate structure that uses a deposited amorphous dielectric film (56). However, experiments have shown unequivocally that even when the devices do not use a deposited dielectric, and consist only of a patterned superconducting film on a high-quality crystalline substrate, a thin, TLS-hosting layer is still present on the surface of the device. As discussed below, the presence of TLS may be diagnosed by measuring the resonator frequency ω_r as a function of temperature and looking for small (typically $\delta\omega_r/\omega_r \sim 10^{-3} - 10^{-6}$) deviations from the Mattis-Bardeen prediction, with a characteristic shape described by a universal function of the dimensionless parameter $\hbar\omega_r/kT$. This behavior is accompanied by an added dissipation that scales with the strength of the anomalous frequency shift and whose temperature dependence also follows a characteristic universal shape. Most notably, the TLS dissipation saturates significantly with increasing measurement power; in contrast, the frequency shift shows only a weak power dependence. This complex behavior is predicted by TLS theory and has now been routinely observed in a wide variety of samples studied by many research groups.

The prevalence of TLS in amorphous materials was proposed four decades ago (68, 69) as a way to explain the anomalous bulk properties (e.g., heat capacity) of these materials at low temperatures. TLS arise due to the random structure of amorphous materials, because occasionally it is possible for an atom or group of atoms to move between two local minima of the potential energy landscape by quantum tunneling over a barrier. The random nature of the amorphous material implies that the potential energy minima and the barrier height are also random, leading to a random, uniform distribution of TLS energy splittings. In general, the TLS are electrically active because the moving atoms carry a dipole moment, and therefore the TLS make a contribution $\varepsilon_{\mathrm{TLS}}(\omega, T)$ to both the real (reactive) and imaginary (dissipative) parts of the dielectric constant ε. In weak fields the loss tangent due to TLS is given by

$$\delta_{\mathrm{TLS}}(\omega, T) = \frac{\mathrm{Im}\,\varepsilon_{\mathrm{TLS}}(\omega, T)}{\mathrm{Re}\varepsilon} = \delta_0 \tanh\left(\frac{\hbar\omega}{2k_B T}\right). \qquad 24.$$

The microwave loss is dominated by TLS with energies $E \approx \hbar\omega$; the familiar hyperbolic tangent factor arises from the thermal occupation probabilities of the two quantum states. For $k_B T << \hbar\omega$, the TLS only occupy the ground state, so $\delta_{\mathrm{TLS}}(\omega, T) \to \delta_0$. The value of δ_0 is proportional to

the density of TLS per unit volume and energy. The earliest models (68, 69) suggested that the low-temperature loss tangent is independent of frequency because the TLS are uniformly distributed in energy; later studies (70) indicate that the distribution function is slowly increasing with energy in the RF and microwave range. In the opposite limit $k_BT << \hbar\omega$, the upper state is well populated and stimulated emission cancels much of the absorption, leading to $\delta_{TLS}(\omega,T) \propto \hbar\omega/k_BT$.

The corresponding behavior of Re $\varepsilon_{TLS}(\omega, T)$ can be found by applying the Kramers-Kronig transform, and causes the resonator frequency to shift by an amount (71, 72),

$$\frac{\delta\omega_r}{\omega_r} = -\frac{F_{TLS}}{2}\frac{\mathrm{Re}\varepsilon_{TLS}(\omega,T)}{\mathrm{Re}\varepsilon} = \frac{F_{TLS}\delta_0}{\pi}\left[\mathrm{Re}\Psi\left(\frac{1}{2}+\frac{1}{2\pi i}\frac{\hbar\omega}{kT}\right) - \ln\frac{\hbar\omega}{kT}\right]. \quad 25.$$

Here, Ψ is the complex digamma function and F_{TLS} is the the fraction of the electric field energy that is contained in the TLS-hosting material. The filling factor F_{TLS} also connects the low-field (unsaturated) resonator dissipation to the TLS loss tangent through $Q_{TLS}^{-1}(\omega,T) = F_{TLS}\delta_{TLS}(\omega,T)$. These predictions of TLS theory have been verified very well in experiments (24, 56, 73, 74), through measurements of the temperature dependence of the resonant frequency and of the quality factor of superconducting microresonators at temperatures $T << T_c$.

For a fixed operating temperature T, a simple way to reduce TLS loss is to operate at low frequencies, $\omega << k_BT/\hbar$. However, the frequency cannot be made arbitrarily low because TLS dissipation increases again below $f_{min} \sim 0.3$ MHz $(T/1\ \mathrm{K})^3$ due to nonresonant relaxation (75). A second method to reduce loss is to use microwave fields that are strong enough to saturate the TLS (76); the expected dependence $\delta_{TLS} \propto [1 + P/P_c]^{-1/2}$ with microwave power P was illustrated nicely by Martinis et al. (56). Neither of these two methods is applicable if the resonator is intended to operate in the quantum-mechanical regime. A third method to reduce TLS loss is to find materials that have a lower TLS density. Martinis et al. (56) showed that SiN_x ($\delta_0 \sim 2 \times 10^{-4}$) could have considerably lower loss than SiO_2 ($\delta_0 \sim 2 \times 10^{-3}$). More recent work (77, 78) has shown that amorphous silicon and silicon-rich SiN_x films deposited using the inductively coupled plasma chemical vapor deposition technique can achieve $\delta_0 \sim 2 \times 10^{-5}$.

Another method for reducing TLS loss is to avoid use of amorphous dielectric films. Indeed, this was the route that led to high-Q CPW resonators, which are fabricated on crystalline substrates. However, even these resonators do have some TLS loss, arising from a thin (a few nanometers) layer on the surface of the device. Although several earlier measurements had strongly pointed to the presence of TLS in such resonators (73, 79), their existence in a 2D layer was established conclusively through geometrical scaling experiments (72) (see **Figure 7**), which made use of the F_{TLS} factor in Equation 25. This layer could be either surface oxides or an adsorbed layer, depending on the materials used, the details of the fabrication, and measurement procedures, etc. The dissipation caused by this surface layer can be reduced by increasing the separation of the electrodes in the capacitive portion of the resonator, because this reduces F_{TLS}. In a recent experiment using NbTiN CPW lines on silicon substrates (80), grooves were etched into the silicon in the CPW slot region. This resulted in $Q_i \sim 4 \times 10^5$ at single-photon excitation levels, about a factor of two improvement relative to their unetched devices. These results suggest that the native oxide at the silicon surface is responsible for a significant portion of the loss.

It should be possible to make a TLS-free capacitor by designing a structure that uses a crystalline dielectric and has no exposed surfaces in regions having a strong electric field. The

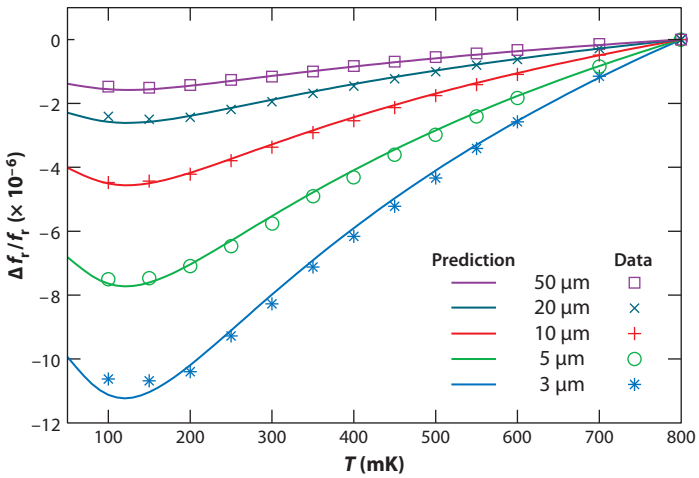

Figure 7

Results of a geometrical scaling experiment demonstrating the existence of a 2D two-level system (TLS) surface layer on niobium-sapphire coplanar-waveguide resonators. The different curves correspond to resonators with varying center strip widths w, as indicated. The measured frequency shift versus temperature (*colored symbols*) closely follows the prediction of TLS theory (*colored lines*; Equation 25), provided that the TLS filling factor scales as $F_{\mathrm{TLS}} \propto w^{-0.9}$, in agreement with conformal mapping calculations. Reprinted with permission from Reference 72. Copyright 2008, American Institute of Physics.

first step toward this ultimate goal was demonstrated recently by Weber et al. (81), who used silicon-on-insulator (SOI) wafers to produce parallel-plate capacitors with a 2-μm-thick layer of crystalline silicon as the dielectric. For capacitance values $C = 2 - 5$ pF, 5-GHz resonator measurements at single-photon excitation levels indicated $Q_i \sim 2 \times 10^5$, corresponding to F_{TLS} $\delta_0 \sim 5 \times 10^{-6}$. At higher drive levels, Q_i increases to $\sim 10^6$, indicating that TLS, perhaps located at the interfaces between the silicon and the aluminum electrodes, are indeed still contributing to the loss. It might therefore be possible to reduce the loss further through improvements to the fabrication process, paying close attention to the condition of the silicon surface prior to metallization.

As a final comment, it is interesting to note the remarkable recent qubit measurements (82) demonstrating energy relaxation (T_1) timescales of $\sim$200 μs. These results indicate that the amorphous aluminum oxide used in the tunnel barrier of the qubit's Josephson junction has a loss tangent of order 4×10^{-8}, which is orders of magnitude lower than the values typically seen in larger-volume samples. As first discussed by Martinis et al. (56), and again by Kim et al. (82), the relevant volume in this case is so small that the discrete nature of the TLS is important. Indeed, the TLS are so few that their average frequency spacing is much larger than the TLS line width; instead of being frequency independent, the loss tangent varies dramatically with frequency. Because of this, it is possible to achieve very low values of loss in the deep valleys in between individual TLS resonances.

5. SUPERCONDUCTING MICRORESONATOR DETECTORS

The demonstration of superconducting microresonators with very high quality factors has opened up numerous new possibilities for superconducting detectors. A wide variety of schemes have been proposed and considered; the common denominator is the use of an array of

microresonators spaced in frequency to allow multiplexed readout. This provides a simple, elegant solution to the long-standing readout problem that has impeded development of large arrays of superconducting detectors. Furthermore, wideband frequency multiplexing has become eminently practical given the advances in high-speed digital signal processing that allow a large number of carrier frequencies to be readily generated and measured by standard room-temperature electronics (83–85).

The simplest scheme is to use the resonator itself as the detector. This approach is commonly known as the microwave kinetic inductance detector (MKID). The physics of MKIDs and a simple model for calculating sensitivity are covered in detail in Sections 5.2 to 5.8; examples of MKIDs are described in Section 5.9. However, we first review a number of important precursors that led to the development of MKIDs.

5.1. Precursors

As mentioned earlier, superconductors have been used for detection for over seven decades. The first devices were bolometers (86) operated on the resistive transition at $T = T_c$. The possibility of a superconducting detector operating at $T << T_c$ was first suggested by Burstein et al. in 1961 (87), who proposed the use of a superconducting tunnel junction to measure the quasiparticles produced by the absorption of energy capable of breaking Cooper pairs. This approach was studied intensively starting in the 1960s with the detection of alpha-particles, and accelerated rapidly in the 1980s and 1990s with detection of X-rays and eventually single optical photons (88). However, interest in these devices has waned due to the difficulty of fabricating ultralow leakage tunnel junctions and the lack of a multiplexed readout scheme.

Another interesting suggestion for $T < T_c$ operation was McDonald's proposal (89) to use the temperature-dependent kinetic inductance for bolometer readout (see **Figure 8**). This device can be understood by writing Equation 2 in the limit $\hbar\omega << \Delta(T)$:

$$\frac{\sigma_2(\omega, T)}{\sigma_n} \approx \frac{\pi\Delta(T)}{\hbar\omega}[1 - 2f(\Delta(T))], \qquad 26.$$

which shows that the temperature dependence of the gap energy $\Delta(T)$ is responsible for the variation of inductance with temperature. The changes in kinetic inductance were to be read out using a superconducting quantum interference device (SQUID) monitoring a bridge circuit excited by a ~100-kHz current (see **Figure 8**). This bridge circuit allows a phase-sensitive measurement scheme: In principle, changes in both the inductance and the resistance (i.e., the complex impedance) of a superconducting meander line could be measured from the variations in the amplitude and phase of the galvanometer's output.

At temperatures far below the transition, $T << T_c$, the temperature variation of the kinetic inductance becomes exponentially small, $\propto e^{-\Delta_0/k_B T}$. However, the kinetic inductance continues to respond in a linear fashion to nonequilibrium changes in the quasiparticle population even as $T \to 0$. The presence of the distribution function $f(\Delta)$ in Equation 26 is a clear indication of this, though we should remember that Δ also responds linearly to $f(E)$ as shown by Equation 4. This point was understood by Bluzer (90), who proposed a detector that used SQUIDs to measure the nonequilibrium changes in kinetic inductance produced by pair-breaking photons. A key aspect of such a device is that the fundamental noise limit is set by the generation-recombination fluctuations of the quasiparticle population, and, in theory, the noise produced by thermal quasiparticles vanishes exponentially with decreasing temperature (91). The dissipative component of the conductivity (σ_1) also responds linearly to nonequilibrium quasiparticles, as is evident from Equation 1. This effect is analogous to the current response of a tunnel

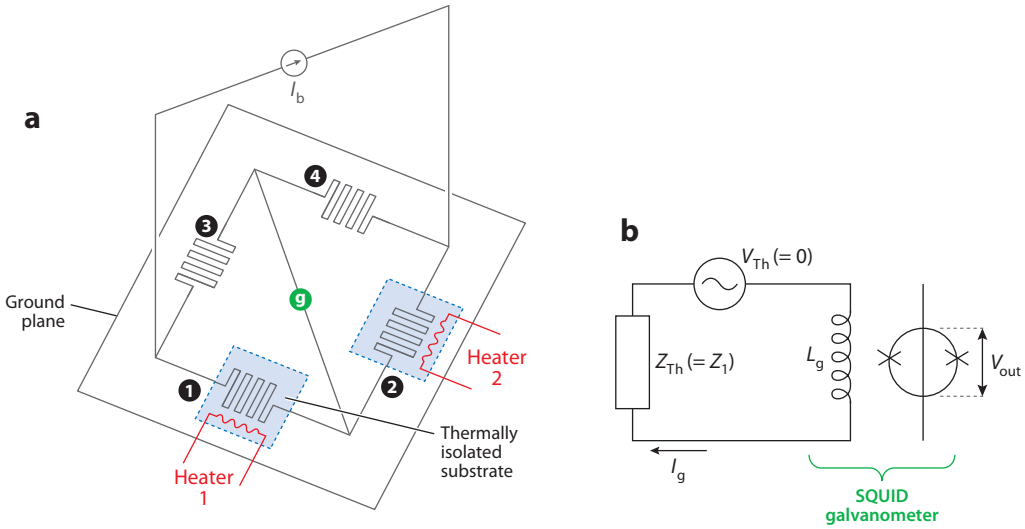

Figure 8

The kinetic inductance thermometer/bolometer proposed by McDonald is shown in panel *a*. The superconducting meander inductors labeled 1, 2, 3, and 4 are arranged in a Wheatstone bridge configuration. Two of the meanders (1, 2) are located on thermally isolated islands (*blue*), whose temperature can be adjusted independently using heaters (*red*). The bridge is excited using an AC generator I_b and is read out using the SQUID galvanometer g (*green*) detailed in diagram *b*. Reprinted with permission from Reference 89. Copyright 1987, American Institute of Physics.

junction detector, as was pointed out by Gulian & Van Vechten (92) and Van Vechten et al. (93). They suggested that X-rays could be detected by illuminating a superconducting film with microwaves and measuring small changes in the reflected power, and discussed the possibility that this response might be enhanced through a positive feedback mechanism involving microwave amplification of the photoproduced quasiparticles.

Clearly, the detector sensitivity is controlled by the ability to measure very small changes in the conductivity $\delta\sigma$. Furthermore, minimizing the superconducting volume is desirable in order to maximize the perturbation $\delta\sigma$ that occurs in response to a fixed energy deposition δE or a change δP in the radiation power absorbed. Both of these points suggest use of superconducting microresonators, and in fact this idea was described by Michael D. Jack in a 1990 patent (94) assigned to the Santa Barbara Research Center. To quote from the patent: "It has been found that Cooper pair breaking by incident photons results in a change in the kinetic inductance and a consequent shift in the resonance frequency of the superconducting transmission line." The patent goes on to describe a readout technique involving use of Schottky-diode detectors to measure the changes in microwave power transmitted through a resonator resulting from the frequency shift, as well as a multiplexing scheme involving coupling each resonator to the readout diode sequentially by means of superconducting critical-current switches. Although the patent is an early recognition of the promise of using superconducting microresonators for detection, the proposed readout scheme is complex and clearly not ideal. The electronics required for simultaneous phase-sensitive readout of a frequency-multiplexed MKID array at noise levels approaching fundamental limits was simply not yet on the horizon in 1990; the wireless communication revolution and the continued validity of Moore's law would soon remove this barrier.

5.2. Microwave Kinetic Inductance Detectors

The MKID concept was developed in 1999 by J. Zmuidzinas and H. G. Leduc, who were motivated by the previous work of Bluzer (90) and Sergeev & Reizer (91). The distinguishing features included the use of superconducting microresonators, a phase-sensitive homodyne readout method using a wideband, low-noise cryogenic amplifier and room-temperature electronics, and multicarrier frequency-domain multiplexing. **Figure 9** depicts the idea as originally conceived. The method of radiation coupling is not shown; the intention was to use an antenna-fed microstrip line to couple submillimeter-wave radiation to the inductor at its center, taking advantage of the microwave virtual ground at that point. Around this time, frequency-domain multiplexing of superconducting detectors was being discussed in other contexts, e.g., in conjunction with radio-frequency single electron transistor (RF-SET) amplifiers following tunnel-junction detectors (95, 96), or as a way of multiplexing transition-edge bolometers (97). In all of these cases, the resonators were elements to be added to the scheme in order to allow multiplexing; in the MKID case, the resonators simultaneously served as detectors, which was a drastic simplification.

In early 2000, measurements of Nb/SiO/Nb microstrip resonators were performed in order to verify that the concept was feasible (see **Figure 4**). As mentioned earlier, the microstrip experiments displayed a number of puzzling effects, such as the variation of the resonator quality factor Q_r with readout power, and half a decade would pass before this behavior was connected to saturation of TLS in the amorphous SiO dielectric (56). Meanwhile, Peter Day suggested switching to CPW resonators (see **Figure 3**) in order to simplify the structure, and by mid-2001 (58) this led to the demonstration of resonators with quality factors around $Q_r \sim 10^6$ (see **Figure 5**). Detection experiments using 6 keV X-rays quickly followed (see **Figure 10**), and in a few years the first journal paper (1) describing and demonstrating the concept was published.

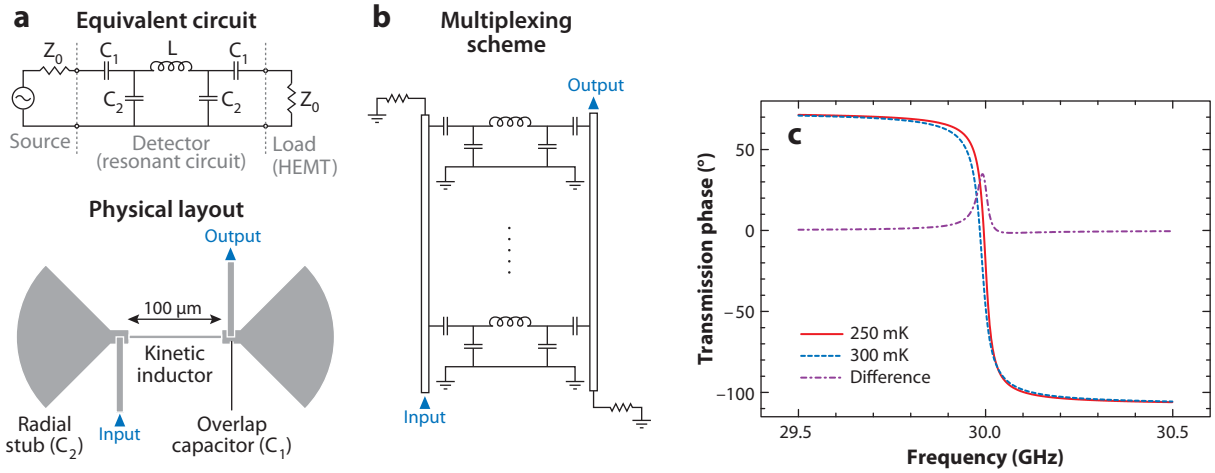

Figure 9

Description of the microwave kinetic inductance detector (MKID) concept as proposed by Zmuidzinas & Leduc in 1999. (*a, top*) An equivalent circuit diagram and (*a, bottom*) a potential physical realization in microstrip. (*b*) Frequency-multiplexed readout of an array of MKIDs using two feedlines. (*c*) Transmission phase response of the proposed circuit, calculated using the Mattis-Bardeen theory. Abbreviation: HEMT, high electron mobility field-effect transistors.

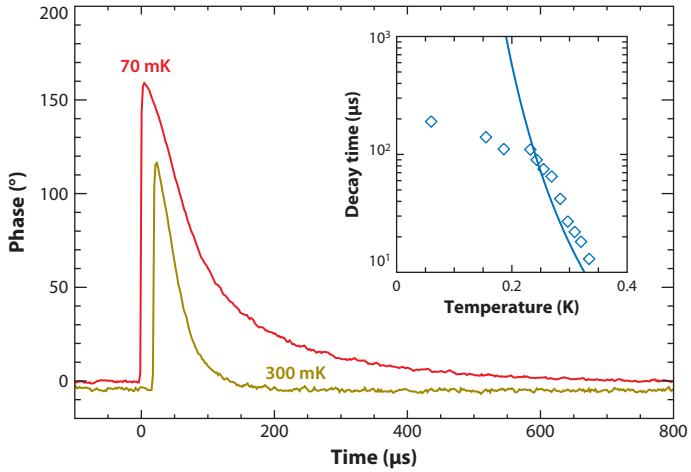

Figure 10

Pulse response of an Al/Al_2O_3 coplanar-waveguide resonator indicating detection of single 5.9-keV X-ray photons. Reprinted with permission from Reference 1.

5.3. Resonator Response

Figure 11 shows the equivalent circuit for an MKID array. Frequency multiplexing is straightforward: The MKID resonators have high impedance away from resonance, so the carrier frequency for a particular MKID is able to propagate past the other MKIDs without interacting. The transmission response (we use the standard scattering matrix description of the circuit response, and S_{21} represents the forward scattering amplitude) of one MKID as a function of frequency is well described by the single-pole approximation,

$$S_{21}(\omega) = 1 - \frac{Q_r}{Q_c}\frac{1}{1 + 2jQ_r x}, \qquad 27.$$

which, by virtue of being a Möbius transformation, maps the real ω axis into a circle in the complex S_{21} plane, as shown in **Figure 11**. Here, $x = (\omega - \omega_r)/\omega_r$ is the fractional detuning of the generator frequency ω from the resonance frequency, Q_c is the coupling quality factor, and Q_r is the resonator quality factor. On resonance, the transmission amplitude reaches its minimum value $\min(|S_{21}|) = 1 - Q_r/Q_c$; far away from resonance, the transmission is unity, $|S_{21}| \to 1$. The value of Q_r may be determined from the resonance linewidth, and recalling Equation 20 we may estimate the coupling and internal quality factors using

$$Q_c = \frac{Q_r}{1 - \min(|S_{21}|)} \qquad 28.$$

and

$$Q_i = \frac{Q_r}{\min(|S_{21}|)}. \qquad 29.$$

Photon absorption in the superconductor results in quasiparticle production and causes the resonance frequency and quality factor to change. For slow variations of these quantities, the change in complex transmission is described by the adiabatic response coefficients,

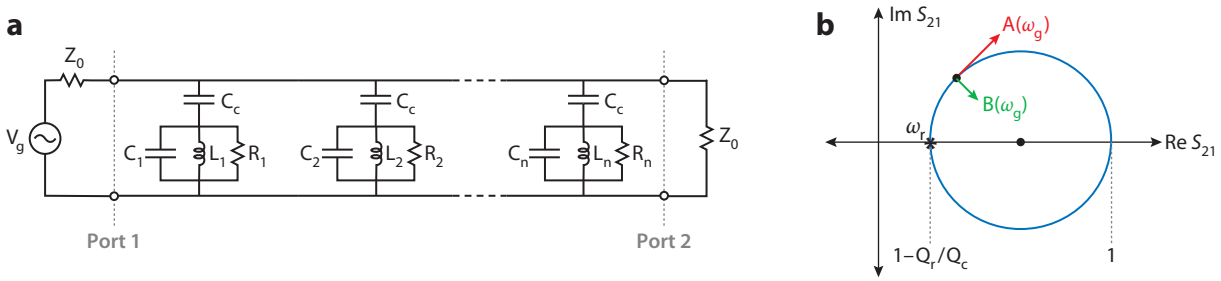

Figure 11

(*a*) A frequency-multiplexed array of shunt-coupled microwave kinetic inductance detectors (MKIDs) is represented by an array of LC resonators with frequencies $\omega_1 = 1/\sqrt{L_1C_1}$, ..., $\omega_n = 1/\sqrt{L_nC_n}$. The straight lines between the resonators represent transmission line sections, and the MKIDs are coupled to this feedline via small capacitances C_c. All MKIDs are driven simultaneously using a multifrequency generator attached to port 1; after propagating past the array, the carriers arrive at port 2 and enter an amplifier represented by the input impedance Z_0. (*b*) For a single resonator, and after compensating for cable delay, the trajectory of the forward scattering amplitude S_{21} as a function of frequency follows a circle in the complex plane. The directions tangent and normal to the resonance circle at a frequency ω_g are represented by the complex numbers $A(\omega_g)$ and $B(\omega_g)$.

$$A(\omega) = -\omega_r \frac{\partial S_{21}}{\partial \omega_r} = +\omega_r \frac{\partial S_{21}}{\partial \omega} = 2jQ_c[1 - S_{21}(\omega)]^2 \quad 30.$$

and

$$B(\omega) = \frac{\partial S_{21}}{\partial Q_i^{-1}} = \frac{1}{2j} A(\omega). \quad 31.$$

The directions of $A(\omega)$ and $B(\omega)$ are tangent and normal, respectively, to the resonance circle, as illustrated in **Figure 11**. Thus, for adiabatic perturbations $\delta x(t)$ and $\delta Q_i^{-1}(t)$ of the resonator detuning and internal dissipation, we may write

$$\delta S_{21}(t) = A(\omega)\delta x(t) + B(\omega)\delta Q_i^{-1}(t). \quad 32.$$

A calculation of the response to more rapid variations of the resonator properties requires that the ring-down response of the resonator be considered. This response is most easily represented as a frequency-domain transfer function,

$$\zeta(\nu, \omega) = \frac{1 - S_{21}(\omega + 2\pi\nu)}{1 - S_{21}(\omega)}, \quad 33.$$

which relates the Fourier transforms of the time-domain quantities,

$$\delta S_{21}(\nu) = \left[A(\omega)\delta x(\nu) + B(\omega)\delta Q_i^{-1}(\nu)\right]\zeta(\nu, \omega). \quad 34.$$

For zero detuning, the resonator transfer function is just a low-pass filter,

$$\zeta(\nu, \omega = \omega_r) = \frac{1}{1 + j2Q_r\nu/\nu_r}, \quad 35.$$

showing that the response rolls off for signal frequencies above the resonator bandwidth, $\nu > \nu_r/2Q_r$. Although ζ is retained in the equations that follow, we usually examine only the adiabatic limit, $\zeta \to 1$, which is valid when $\nu << \nu_r/2Q_r$.

It is convenient to express the adiabatic response coefficients in terms of their maximum values for zero detuning and optimum coupling $Q_c = Q_i = 2Q_r$. We introduce the phase angle,

$$\phi_g = \tan^{-1} 2Q_r x, \tag{36.}$$

the coupling efficiency factor,

$$\chi_c = \frac{4Q_c Q_i}{(Q_c + Q_i)^2} \leq 1, \tag{37.}$$

which reaches unity for optimum coupling $Q_c = Q_i$, and also the detuning efficiency,

$$\chi_g(\omega) = \frac{1}{1 + 4Q_r^2 x^2} \leq 1, \tag{38.}$$

which is maximized when the generator is tuned to the center of the resonance, $\omega = \omega_r$. Using this notation, we may write

$$A(\omega) = j\frac{Q_i}{2}\chi_c \chi_g e^{-2j\phi_g} \tag{39.}$$

and

$$B(\omega) = \frac{Q_i}{4}\chi_c \chi_g e^{-2j\phi_g}. \tag{40.}$$

Amplifier noise may be accounted for by adding a noise term to Equation 34. This describes the additive noise of the amplifier, as characterized by its noise temperature T_a. Depending on the readout carrier power, signal bandwidth, and the gain stability of the amplifier, multiplicative noise due to variations in the amplifier's complex gain (amplitude and phase) may also need to be considered. Fortunately, a variety of mitigation strategies (e.g., pilot tones interspersed between the readout tones, carrier suppression techniques, or more rapid signal modulation) may be deployed, so we assume that it is safe to ignore such effects. Including the amplifier's additive noise, we may write

$$\delta S_{21}(v) = \frac{1}{4}\chi_c \chi_g Q_i e^{-2j\phi_g}\left[2j\delta x(v) + \delta Q^{-1}(v)\right]\zeta(v, \omega) + \delta S_a(v). \tag{41.}$$

Here, $\delta S_a(t) = \delta I_a(t) + j\delta Q_a(t)$ is the fluctuation in the measured forward transmission caused by the amplifier noise, and is characterized by

$$\langle \delta I_a(v)\delta I_a^*(v')\rangle = \langle \delta Q_a(v)\delta Q_a^*(v')\rangle = \frac{kT_a}{2P_g}\delta(v - v'); \tag{42.}$$

all other correlations vanish. As expected, the signal-to-noise ratio in the transmission measurement improves with the generator power P_g. Note that a portion of the generator power is absorbed in the resonator, given by $P_a = \chi_a P_g$, where the absorption efficiency is

$$\chi_a(\omega) = \frac{\chi_c \chi_g(\omega)}{2} \leq \frac{1}{2}. \tag{43.}$$

5.4. Noise from Two-Level Systems

In practice, superconducting microresonators are found to have excess frequency noise (1, 67, 73, 79, 98) varying with frequency as $\sim f^{-1/2}$ and corresponding to transmission perturbations in a direction that is purely tangential to the resonance circle (see **Figure 12**). Amazingly, noise in the perpendicular direction corresponding to dissipation fluctuations is not seen even at levels well below the standard quantum limit (99). For

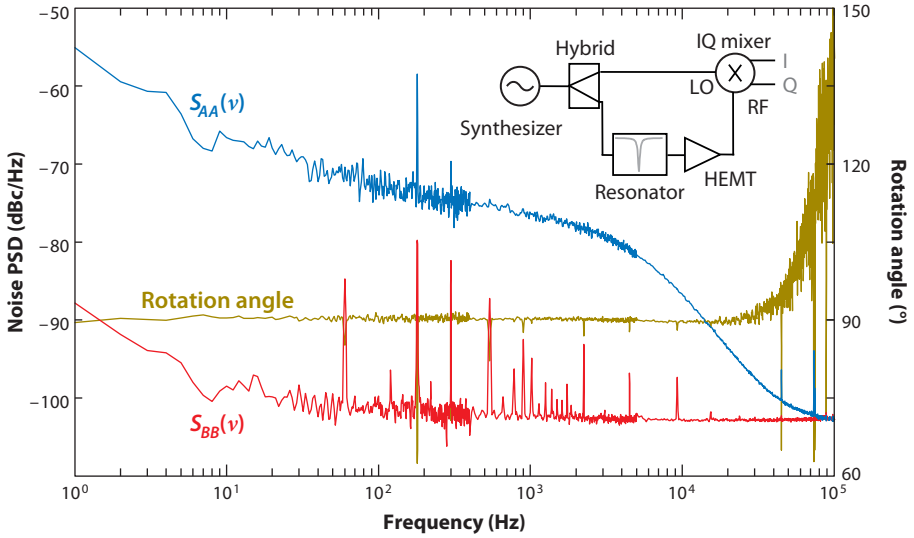

Figure 12

This figure illustrates two-level system (TLS) frequency noise in a 4.4-GHz Nb/Si superconducting microresonator. The inset shows the standard IQ homodyne measurement scheme used to measure the complex forward transmission $S_{21} \propto I + jQ$. At a fixed generator frequency $\omega = \omega_r$, noise fluctuations δS_{21} are projected into the directions tangent and perpendicular to the resonance circle, as indicated by the vectors A and B shown in **Figure 11**. The blue line shows $S_{AA}(\nu)$, the noise power spectral density (PSD) in the frequency (tangent) direction A, and is dominated by TLS noise, rolled off above 6 kHz by the resonator's response function $|\zeta(\nu,\omega_r)|^2$. The red line shows $S_{BB}(\nu)$, the noise in the dissipation direction B, and is limited by amplifier noise. The dark yellow line shows the measured rotation angle between the major principal axis of the noise ellipse and the dissipation direction B. The fractional frequency noise PSD is given by $S_{\rm TLS}(\nu) = S_{\rm AA}(\nu)Q_c^2/4Q_r^4$;$Q_r = Q_c = 3.5 \times 10^5$ for this example. Reprinted with permission from Reference 79. Copyright 2007, American Institute of Physics. Abbreviation: HEMT, high electron mobility field-effect transistors.

CPW resonators on crystalline substrates, this noise is caused by TLS in a thin amorphous dielectric surface layer that is known to exist from frequency-shift studies (72). Experiments (100) have definitively shown that the noise is due to the resonator's capacitor, not the inductor: The noise may be reduced by a large factor by increasing the electrode separation in the capacitor (reducing $F_{\rm TLS}$), while leaving the inductor unchanged. Parallel-plate capacitors using single-crystal silicon dielectrics (81) may also provide a route to reduced TLS noise. The fractional frequency perturbation $\delta x_{\rm TLS}$ produced by this mechanism enters the response equation in exactly the same way as the desired kinetic inductance signal δx,

$$\delta S_{21}(\nu) = \frac{1}{4}\chi_c\chi_g Q_i e^{-2j\phi_g}\zeta(\nu,\omega) \times \left[2j\delta x(\nu) + 2j\delta x_{\rm TLS}(\nu) + \delta Q^{-1}(\nu)\right] + \delta S_a(\nu). \quad 44.$$

The spectral density $S_{\rm TLS}(\nu)$ of $\delta x_{\rm TLS}$ is observed (73) to vary with readout power as $P_g^{-1/2}$ and with temperature as $T^{-\beta}$ with $\beta = 1.5 - 2$ (see **Figure 13**). Unfortunately, a microscopic theory for TLS frequency noise is not yet available; the only tool at hand is the semiempirical model of Gao et al. (98). In this model, the fractional frequency noise is given by

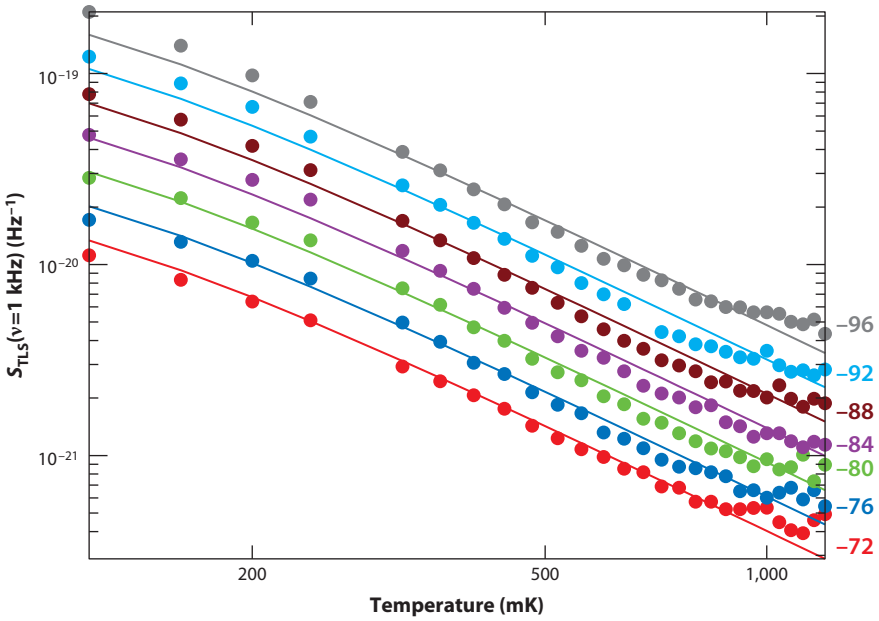

Figure 13

This figure illustrates the dependence of two-level systems (TLS) frequency noise with temperature and readout power. The fractional frequency noise $S_{TLS}(\nu = 1\ kHz)$ of a 4.4-GHz Nb/Si coplanar-waveguide resonator varies as $\sim T^{-1.7}$ over the 0.1–1-K temperature range. The numbers on the right indicate the microwave readout power P_g in decibels referenced to one milliwatt; the noise scales as $S_{TLS} \propto P_g^{-0.5}$. The readout power can be converted to internal power using (24) $P_{int} = (2Q_r^2/\pi Q_c)P_g$. For this device, $Q_r \approx Q_c = 5 \times 10^5$. Reprinted with permission from Reference 73. Copyright 2008, American Institute of Physics.

$$S_{TLS}(\nu) = \kappa(\nu, \omega, T) \frac{\int_{V_{TLS}} |\vec{E}(\vec{r})|^3 d^3\vec{r}}{4\left(\int_V |\epsilon(\vec{r})\vec{E}(\vec{r})|^2 d^3\vec{r}\right)^2}, \qquad 45.$$

where $\kappa(\nu, \omega, T)$ captures the $\nu^{-1/2}$ spectral shape as well as the dependence on microwave frequency and temperature, $\vec{E}$ is the microwave electric field, $\epsilon(\vec{r})$ is the dielectric constant, V_{TLS} is the volume in which the TLS exist, and V is the total volume. The numerical values of S_{TLS} obviously depend on the construction of the capacitor and scale inversely with the operating voltage. Values around 10^{-18} Hz^{-1} at $\nu = 1$ Hz and 10^{-20} Hz^{-1} at $\nu = 1$ kHz have been demonstrated using interdigitated capacitors ($C = 2$ pF) on silicon substrates with 0.7 mm^2 area, 10 μm finger width and separation, and operated at $\omega/2\pi = 5.6$ GHz, $P_{int} \approx -50$ dBm, and $T = 120$ mK (100). Under these conditions, the r.m.s. capacitor voltage is around 1.3 mV and the average resonator energy is 3×10^{-18} J, equivalent to 10^6 microwave photons. By using NbTiN superconducting films and etching the silicon substrate in the CPW slot region, Barends et al. (101) have demonstrated $S_{TLS}(1\ kHz) = 2 \times 10^{-21}$ Hz^{-1} at 310 mK, –30 dBm ($\sim 10^8$ photons), and 3–5 GHz (see **Figure 14**). Accounting for the higher temperature and operating power, this noise level is roughly an order of magnitude higher than that shown by Noroozian et al. (100) but was accomplished using a device with considerably smaller area. Based on their experimental results and analysis, Barends et al. argue that the exposed (and presumably oxidized) areas of the silicon substrate in the high-field CPW slot region, rather than the NbTiN

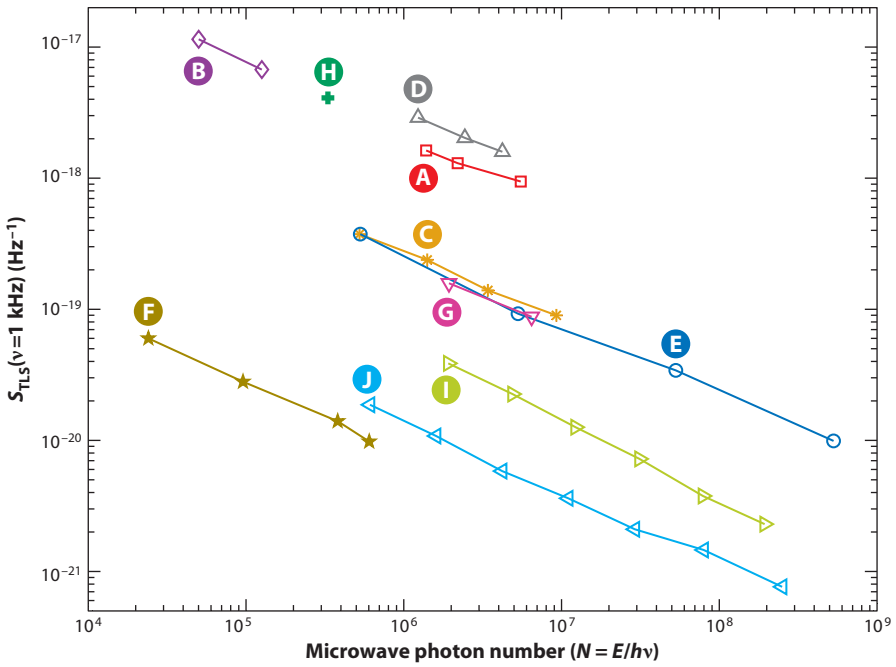

Figure 14

The two-level system fractional frequency noise measured at 1 kHz for a variety of resonators is plotted as a function of the stored microwave energy measured in photon units, $N = E/h\nu_r$. The data are as follows: (A) 320 nm Al on Si, w=3 μm and g=2 μm coplanar waveguide (CPW) (see **Figure 3**; abbreviated to 3-2), $\nu_r = 5.8$ GHz, T=120 mK (79); (B) 40 nm Al on Si, 3-2, 4.8 GHz, 120 mK (79); (C) 200 nm Al on sapphire, 3-2, 4 GHz, 120 mK (79); (D) 200 nm Al on Ge, 3-2, 8 GHz, 120 mK (79); (E) 200 nm Nb on Si, 3-2, 5.1 GHz, 120 mK (79); (F) 200 nm Nb IDC on Si with 60 nm Al 6-2 CPW inductor, 5.6 GHz, 120 mK (100); (G) 40 nm TiN ($T_c = 4.5$ K) on Si, 3-2, 6 GHz, 100 mK (61); (H) 4-μm-wide microstrip, 93 nm Al + 200 nm a-Si:H + 154 nm Al, 9 GHz, ∼150 mK; (I) 300 nm NbTiN on Si, 3-2, 4.4 GHz, 310 mK (101); (J) 300 nm NbTiN on Si, 6-2, 2.64 GHz, 310 mK (101).

surfaces, are responsible for a significant portion of the noise. TLS noise spectra for other geometries and materials and an estimate for $\kappa(\nu, \omega, T)$ for amorphous films may be found in J. Gao's PhD thesis (24). Much work remains to be done in this area to explore alternative capacitor geometries, materials, and operating conditions, and especially to develop a viable microscopic theory of the noise.

5.5. Nonlinear Response

In order to reduce TLS noise and to overcome amplifier noise, it is desirable to use a microwave readout power that is as large as possible. Consequently, MKIDs are usually operated in a regime in which the microwave currents are strong and nonlinearity is becoming important. It has long been known that superconductors exhibit a nonlinear response (102, 103). For $T << T_c$, we may write an expansion of the kinetic inductance L_k of a superconducting strip in terms of the current:

$$L_k(I) = L_k(0)\left(1 + \frac{I^2}{I_2^2} + \ldots\right), \qquad 46.$$

where we recognize that the linear term must vanish due to symmetry considerations. Here, I_2 sets the scale of the quadratic nonlinearity and is expected to be of order the critical current. One manifestation of this effect is that the resonance frequency may shift with magnetic field because magnetic fields may induce circulating currents. This is especially important for CPW resonators, for which the extended superconducting ground plane acts to focus flux lines into the narrow CPW slot regions where the influence on the resonator is strongest. This effect was studied experimentally by Healey et al. (104), who found a $|\vec{B}|^2$ dependence of the resonance frequency with magnetic field, as expected from Equation 46. This is a nuisance for some practical applications such as telescope instruments that move in the Earth's field (105). Such effects may be minimized by using resonator geometries that do not support circulating currents and do not have large ground planes covering the surface of the substrate. One example is the lumped-element resonator shown in **Figure 1**.

In the limit that the film is thin compared to its penetration depth, we may use Equation 5 to express the surface inductance as

$$L_s = \frac{\hbar R_s}{\pi \Delta_0} = \frac{\hbar}{\pi \Delta_0} \frac{\rho_n}{t}, \qquad 47.$$

where t is the film thickness, as before. A strip of length l and width w has a kinetic inductance of $L_k = L_s(l/w)$, volume $V = lwt$, and pairing energy $E_p = 2N_0\Delta_0^2 V$. We expect the fractional change in inductance due to the nonlinearity to be of order the ratio of the inductive energy to the pairing energy:

$$\frac{\delta L_k}{L_k} = \frac{I^2}{I_2^2} = \kappa_* \frac{L_k I^2}{E_p} = \kappa_* \frac{J^2}{J_*^2}, \qquad 48.$$

where κ_* is a dimensionless constant of order unity, $J = I/(wt)$ is the current density, and

$$J_* = \sqrt{\frac{\pi N_0 \Delta_0^3}{\hbar \rho_n}}. \qquad 49.$$

A more rigorous discussion of the nonlinearity, based on the BCS theory, was given by Parmenter (106). Anthore et al. (107) presented tunneling measurements of the density of states of a current-carrying superconductor as well as a comparison to calculations using the Usadel equations. They find that the gap varies quadratically with current according to

$$\frac{\Delta}{\Delta_0} \approx 1 - 0.95 \frac{J^2}{J_*^2}, \qquad 50.$$

suggesting that $\kappa_* = 0.95$. The critical current density is $J_c \approx 0.42\, J_*$, in agreement with Romijn et al. (108). Another useful resource on this topic is the recent paper of Annunziata et al. (108a), who compare their measurements of the nonlinear kinetic inductance for Nb and NbN devices to the predictions of both Ginzburg-Landau and BCS theories.

The kinetic inductance nonlinearity gives rise to classic Duffing oscillator behavior. The stored energy in the oscillator is given by

$$E = \frac{\chi_c}{2} \frac{1}{1 + 4Q_r^2 x'^2} \frac{Q_i P_g}{\omega_r}, \qquad 51.$$

except that now the fractional detuning x' must account for the fact that the resonator frequency shifts downward as a result of the nonlinear inductance:

$$x' = \frac{\omega - \omega_r}{\omega_r} + \frac{E}{E_*}, \qquad 52.$$

where the nonlinear energy scale is $E_* = 2L_k I_*^2/\alpha\kappa_*$. Here α is the kinetic inductance fraction. **Figure 15** shows the result of solving Equations 51 and 52 simultaneously: As the readout power is increased, the resonance becomes distorted and asymmetric, and eventually bifurcates. Note that the resonance depth is predicted to stay constant: This is a signature of a purely reactive nonlinearity. This behavior is expected theoretically for the intrinsic nonlinearity of a superconductor and is indeed observed for resonators made with high-quality films and operated at $T << T_c$. Such behavior is highly desirable for low-noise applications such as parametric amplification (50, 51, 109). However, in other cases the resonator dissipation may be nonlinear, increasing with the stored energy; in that case, the resonance becomes shallower as the resonator is driven harder. The niobium microstrip resonator measurements presented by Golosovsky et al. (110) provide an example of the latter case; they argue that vortex penetration is the likely mechanism for the nonlinear dissipation for their devices. Meanwhile, nonlinear behavior seen in NbN resonators has been interpreted in terms of a grain-boundary weak-link heating model (111). Quasiparticles also provide an important mechanism for nonlinearity if their population is not negligible. This is often the case for MKIDs due to the photoproduction of quasiparticles. Microwave heating of the quasiparticle population can change the dissipative conductivity σ_1, and if the microwave power dissipation is high enough, quasiparticle production is possible, changing both σ_1 and σ_2. A simple thermal model providing a preliminary treatment of such effects is presented in (112) and is compared qualitatively to measurements.

5.6. MKID Optical Response

5.6.1. Feedback due to nonlinearity. In order to calculate the optical response of an MKID, it is necessary to make a connection between a perturbation in the optical power absorbed, δP_o, and the resulting frequency and dissipation perturbations, δx and δQ_i^{-1}. The resulting perturbation of the resonator transmission may then be calculated using Equation 32. If operating conditions are such that the kinetic inductance nonlinearity (Equation 46) is significant, we would need to use a modified version of this equation,

$$\delta S_{21} = A(\omega)\delta x' + B(\omega)\delta Q_i^{-1}, \qquad 53.$$

where now the fractional frequency shift incorporates feedback effects that result from the nonlinearity,

$$\delta x' = \left[1 + \frac{8ay}{(1+4y^2)^2}\right]^{-1}\left[\delta x - \frac{2a}{(1+4y^2)^2}\delta Q_i^{-1}\right]. \qquad 54.$$

Here a is the nonlinearity parameter defined in **Figure 15**, $y = Q_r x'$, and x' is given by Equation 52. The standard linear response $\delta x' = \delta x$ is recovered if a $\rightarrow 0$ or y $\rightarrow \infty$, as expected. Note that the kinetic inductance nonlinearity acts only to modify the response in the direction A tangent to the resonance circle; the response in the radial direction B is not affected. Furthermore, at the center of the nonlinear resonance $y \rightarrow 0_+$, which is experimentally accessible, we have $\delta x' = \delta x - 2a\delta Q_i^{-1}$, indicating that the frequency response is reduced and may even change sign if a is large enough. For simplicity, we ignore this nonlinearity and use Equation 32 to calculate MKID response. While this approach gives correct results for the dissipation response, the amplifier noise will in general be underestimated for frequency readout of devices

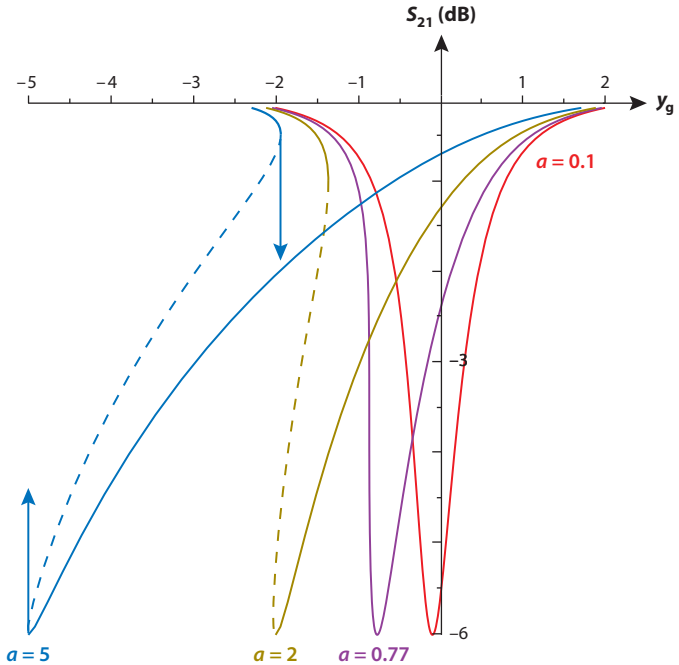

Figure 15

This plot shows the power transmission $|S_{21}|^2$ as a function of the normalized generator detuning $y_g = Q_r(\omega - \omega_r)/\omega_r$ for various values of the nonlinearity parameter $a = (2Q_r^3/Q_c\omega_r E_*)P_g$. For $a > 4\sqrt{3}/9 \approx 0.77$, the resonance enters the bifurcation regime, and the response exhibits discontinuous jumps as indicated by the arrows. The dashed portions of the resonance curves are not experimentally accessible. The resonances are plotted for the case $\chi_c = 1$ ($Q_i = Q_c$); this choice governs the value of the transmission minimum (-6 dB).

operated deep into the nonlinear kinetic inductance regime, so appropriate corrections should be included for that case.

5.6.2. The quasiparticle system: a simplified treatment. At present, a fully rigorous method for calculating δx and δQ_i^{-1} from δP_o has not been developed, so we adopt a simplified approach in which we characterize the state of the superconductor by specifying the number (or density) of quasiparticles. A more rigorous calculation would include finding the steady-state quasiparticle distribution function $f(E)$ as well as the perturbation $\delta f(E, t)$ that occurs in response to a time-dependent perturbation $\delta P_o(t)$, taking taking into account the fact that the quasiparticle system is absorbing both optical and microwave power because both effects are capable of heating the quasiparticle system as well as breaking pairs to produce more quasiparticles. The Chang-Scalapino equations (21) governing the distribution functions of the coupled quasiparticle-phonon system provide one possible approach for performing this calculation, and this route is being pursued. One possible worry is that, according to Equation 50, the gap is varying in a time-dependent way and such effects are not included in the Chang-Scalapino formalism. MKIDs are typically operated in a regime in which the frequency shift due to the nonlinearity is of order the linewidth, $\Delta\omega/\omega_r \sim Q_r^{-1} < 10^{-4}$. Dividing by the kinetic inductance fraction gives the fractional modulation of the gap, $|\Delta - \Delta_0|/\Delta_0 \sim Q_r^{-1}/\alpha \sim$ few $\times\, 10^{-3}$. Meanwhile, the quasiparticle energy levels that are relevant for the conductivity extend at least $\sim\hbar\omega$ above

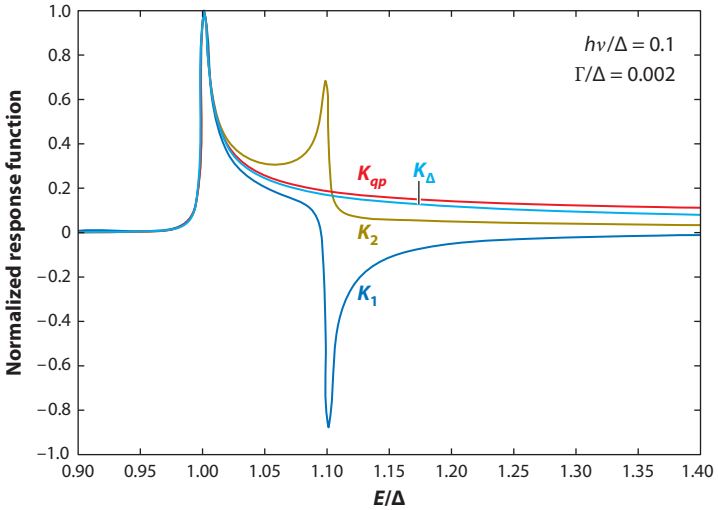

Figure 16

This plot illustrates the response functions that describe how the quasiparticle density (K_{qp}), energy gap (K_Δ), and complex conductivity (K_1 and K_2) respond to the quasiparticle distribution function $f(E)$. For the purpose of display, the response functions have been arbitrarily normalized to unity at $E = \Delta_0$, and an arbitrary value of the energy broadening parameter $\Gamma/\Delta_0 = 0.002$ has been used to soften the gap-edge singularities (see Equation 19).

the gap, and typically $\hbar\omega/\Delta_0 > 10^{-2}$. Thus, the modulation of the gap energy with current could have a noticeable but not dominant effect on the quasiparticle dynamics.

Because MKIDs are operated at $T << T_c$, the distribution function is small, $f(E) << 1$. The perturbation of any physical quantity X away from its zero-temperature value $X(0)$ may therefore be calculated to first order using an expression of the form

$$X - X(0) = \int_{\Delta_0}^{\infty} K_X(E) f(E) = \langle K_X | f \rangle ; \qquad 55.$$

the second expression is the familiar Dirac notation for the inner product between the response function $K_X(E)$ and the distribution function $f(E)$. Using Equations 1–4, expressions for the response functions for the conductivity, quasiparticle density, and gap may be worked out. These response functions are shown in **Figure 16**; care must be taken when working out the expression for K_2 because the first-order variation in Δ must be included. Once the steady-state distribution $f(E)$ is in hand, we may apply a perturbation δP_o to the optical power and work out the response $\delta f(E)$ in the distribution function, and from there the perturbation to any physical quantity,

$$\delta X = \langle K_X | \delta f \rangle . \qquad 56.$$

As mentioned earlier, calculating $f(E)$ or $\delta f(E)$ would in general require solving the kinetic equations (21) governing the distribution functions of the coupled quasiparticle-phonon system. We instead turn to a simplified model in which we use only a single variable to describe the system, the quasiparticle number $N_{qp} = \langle K_{qp} | f \rangle$, rather than the full distribution function $f(E)$. We do not need to make any assumptions about the specific form of $f(E)$, and in particular $f(E)$ need not follow a thermal distribution. However, we make the simplifying assumption that any perturbation in the optical power δP_o will lead to a

perturbation in the quasiparticle distribution that has the same shape as the steady-state distribution, $\delta f(E) \propto f(E)$. Although this assumption is a reasonable starting point, it is not guaranteed to be correct, and this is an important topic for future research. Our assumption guarantees that the fractional perturbations to the physical quantities are all equal, because

$$\frac{\delta X}{X - X(0)} = \frac{\langle K_X | \delta f \rangle}{\langle K_X | f \rangle} = \frac{\langle K_Y | \delta f \rangle}{\langle K_Y | f \rangle} = \frac{\delta Y}{Y - Y(0)}. \quad 57.$$

Thus, we can reduce the problem to the calculation of $\delta N_{qp}/N_{qp}$.

5.6.3. Quasiparticle lifetime. The quasiparticle population may be calculated by balancing the generation and recombination rates. Quasiparticles recombine via phonon emission along with the subsequent escape of the recombination phonon from the superconducting volume (113). Superconducting microresonators have proven very valuable for studying this process (114, 115). As illustrated in **Figure 17**, experimentally, the quasiparticle lifetime τ_{qp} varies with thermal quasiparticle density in a manner that is fairly well described by the relation

$$\tau_{qp} = \frac{\tau_{\max}}{1 + n_{qp}/n^*}, \quad 58.$$

where the crossover density $n^* \sim 100\ \mu\text{m}^{-3}$ is observed to be roughly constant for a wide range of materials, and $\tau_{\max}$ is the experimentally observed maximum lifetime. The physics governing

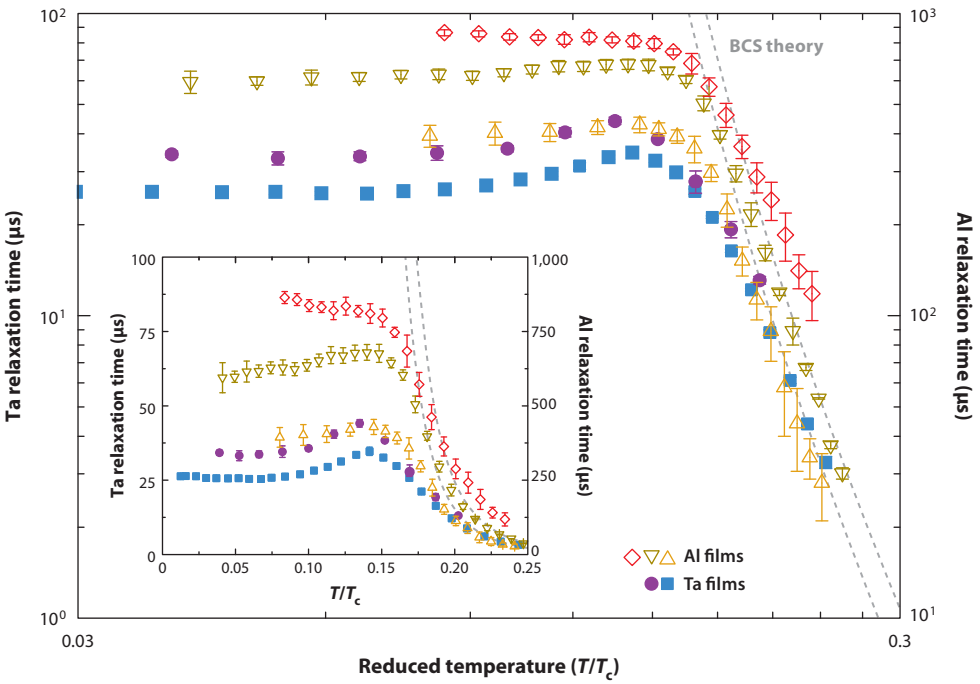

Figure 17

This figure shows the beautiful quasiparticle lifetime measurements made using superconducting microresonators. The filled symbols represent Ta films; the open symbols are Al films. The inset shows the same data on a linear scale. Reprinted with permission from Reference 114. Copyright 2008, American Physical Society.

n^* and τ_{max} is not yet understood; typical values are $\tau_{max} = 100$–$1{,}000$ μs for materials with $T_c \sim 1$ K.

In a recent study, the transmission fluctuations δS_{21} observed in an Al CPW resonator were interpreted in terms of the random generation and recombination of quasiparticles (116). The intensity and bandwidth of these fluctuations were used to infer an equivalent quasiparticle density of around $n_{qp} \approx 50\ \mu m^{-3}$ at the lowest temperatures, consistent with the observed value of τ_{max}. It is therefore plausible that the lifetime is limited by excess quasiparticles, as the authors argue. However, this excess population requires power dissipation in the superconductor to be maintained, and the source of this dissipation is not clear. Furthermore, the results for Ta shown in **Figure 17** cannot also be explained in the same way, because the power dissipation required to maintain an excess population indicated by the value of τ_{max} is orders of magnitude larger for Ta. Furthermore, in an effort to study whether trapping of quasiparticles into localized states near magnetic impurities (117) could be responsible for the lifetime saturation, Barends et al. (115) measured the lifetimes for Ta and Al films ion-implanted with Mn, Ta, and Al. They observed a clear, systematic reduction in τ_{max} with ion concentration; however, self-implantation (e.g., Al into Al) gave about the same reduction as Mn implantation. This result may indicate that τ_{max} is sensitive to disorder in the material; in any case, it seems rather unlikely that a residual quasiparticle population controls the value of τ_{max} observed, except possibly for the cleanest of the Al samples. Thus, despite the substantial progress made over the past several years, our understanding of quasiparticle dynamics remains incomplete.

5.6.4. Quasiparticle generation and recombination. Equation 58 implies that the recombination rate is given by

$$\Gamma_r = \frac{N_{qp}}{\tau_{max}}\left(1 + \frac{N_{qp}}{2N^*}\right), \qquad 59.$$

where $N_{qp} = n_{qp}V$ is the number of quasiparticles in the active volume V of the MKID, and $N^* = n^*V$. By equating quasiparticle generation and recombination rates, the quasiparticle density is calculated to be

$$n_{qp}(T,\Gamma) = \sqrt{\left(n_{th}(T) + n^*\right)^2 + 2\Gamma\tau_{max}n^*/V} - n^*. \qquad 60.$$

Here, $\Gamma(P_a, P_o)$ is the quasiparticle generation rate that results from absorption of optical and microwave power and $n_{th}(T)$ is the thermal equilibrium quasiparticle density. The optimum case is to operate at temperatures low enough so that $n_{th}(T) << n_{qp}$, yielding

$$\frac{n_{qp}}{n^*} = \sqrt{1 + 2\Gamma\tau_{max}/N^*} - 1. \qquad 61.$$

In this limit,

$$\tau_{qp} = \frac{\tau_{max}}{\sqrt{1 + 2\Gamma\tau_{max}/N^*}}. \qquad 62.$$

The perturbation in the quasiparticle number δN_{qp} in response to a change δP_o in the optical power is therefore given by

$$\delta N_{qp} = \frac{\partial N_{qp}}{\partial P_o}\delta P_o = \frac{\eta_o\tau_{qp}}{\Delta_0}\delta P_o, \qquad 63.$$

where we have defined η_o as the efficiency with which optical power creates quasiparticles, $\partial\Gamma/\partial P_o = \eta_o/\Delta_0$. Conservation of energy implies $\eta_o \leq 1$; typically we might expect $\eta_o \sim 0.7$. In this calculation, we have assumed that the absorbed microwave power P_a remains constant. In fact, there is a feedback effect: The increase in the number of photoproduced quasiparticles causes P_a to increase, leading to further quasiparticle production. This is the quasiparticle amplification discussed by Gulian & Van Vechten (92), and is analogous to positive electrothermal feedback in a bolometer. It can be shown (see Section 5.7) that the feedback vanishes for an optimized detector, when quasiparticles dominate the internal dissipation and when the coupling is optimized, $\chi_c = 1$.

5.6.5. Resonator response. We now turn our attention to the resonator response. A perturbation in the resonator inductance δL causes a perturbation in the detuning δx given by

$$\delta x = \delta L/2L(0) = \alpha\delta X_s/2X_s(0), \tag{64.}$$

where α is the kinetic inductance fraction, as before. Meanwhile, the internal quality factor due to quasiparticle losses is

$$Q_{qp}^{-1} = \alpha R_s/X_s(0). \tag{65.}$$

The surface impedance may be calculated using Equation 13:

$$Z_s = Z_s(0) - \gamma Z_s(0)\frac{\sigma - \sigma(0)}{\sigma(0)}. \tag{66.}$$

Because $Z_s(0) = jX_s(0)$ and $\sigma(0) = -j\sigma_2(0)$, the real and imaginary parts of this equation yield

$$R_s = \gamma X_s(0)\langle\tilde{K}_1\,|f\rangle, \tag{67.}$$

$$\delta X_s = \gamma X_s(0)\langle\tilde{K}_2\,|\,\delta f\rangle, \tag{68.}$$

where $\tilde{K}_{1,2}(E) = K_{1,2}(E)/\sigma_2(0)$ are the dimensionless conductivity response functions. We may also introduce a dimensionless quasiparticle response function: $\tilde{K}_{qp}(E) = K_{qp}(E)/2N_0\Delta_0$. Thus, we arrive at

$$\delta x = \frac{\alpha\gamma}{2}\langle\tilde{K}_2\,|\,\delta f\rangle = \frac{\alpha\gamma}{2}\frac{\langle\tilde{K}_2\,|f\rangle}{\langle\tilde{K}_{qp}\,|f\rangle}\langle\tilde{K}_{qp}|\delta f\rangle = \alpha\gamma\frac{\langle\tilde{K}_2\,|f\rangle}{\langle\tilde{K}_{qp}\,|f\rangle}\frac{\delta N_{qp}}{4N_0\Delta_0 V} \tag{69.}$$

and

$$Q_{qp}^{-1} = \alpha\gamma\langle\tilde{K}_1\,|f\rangle = 2\alpha\gamma\frac{\langle\tilde{K}_1\,|f\rangle}{\langle\tilde{K}_{qp}\,|f\rangle}\frac{N_{qp}}{4N_0\Delta_0 V}. \tag{70.}$$

This makes it convenient to define

$$S_1(\omega) = \frac{\langle\tilde{K}_1\,|f\rangle}{\langle\tilde{K}_{qp}\,|f\rangle} = \frac{2}{\pi}\sqrt{\frac{2\Delta_0}{\pi k_B T}}\,\sinh\left(\hbar\omega/2k_BT\right)K_0(\hbar\omega/2k_BT), \tag{71.}$$

$$S_2(\omega) = \frac{\langle\tilde{K}_2\,|f\rangle}{\langle\tilde{K}_{qp}\,|f\rangle} = 1 + \sqrt{\frac{2\Delta_0}{\pi k_B T}}\,\exp\left(-\hbar\omega/2k_BT\right)I_0\left(\hbar\omega/2k_BT\right), \tag{72.}$$

where the explicit expressions apply for a thermal distribution.

If we combine these results with Equation 44, we obtain

$$\delta S_{21}(\nu) = \frac{1}{4}\chi_c\chi_g\chi_{qp}e^{-2j\phi_g}[1 + j\beta(\omega)]\zeta(\nu,\omega)\frac{\delta N_{qp}(\nu)}{N_{qp}} + je^{-2j\phi_g}\frac{\chi_c\chi_g}{2}Q_i\zeta(\nu,\omega)\delta x_{\mathrm{TLS}}(\nu) + \delta S_a(\nu), \quad 73.$$

where

$$\beta(\omega) = \frac{\langle K_2\,|f\rangle}{\langle K_1\,|f\rangle} = \frac{S_2(\omega)}{S_1(\omega)} = \frac{\langle K_2\,|\delta f\rangle}{\langle K_1\,|\delta f\rangle} = \frac{\delta\sigma_2}{\delta\sigma_1} \quad 74.$$

describes the ratio of the response tangent to and normal to the resonance circle, and $\chi_{qp} = Q_i/Q_{qp} \leq 1$ is the fraction of the resonator internal dissipation contributed by the quasiparticles. It is straightforward to calculate $\beta(\omega, T)$ for a thermal distribution; the result is shown in **Figure 18**. However, we must remember that $f(E)$ may not necessarily be well described by a thermal distribution for an MKID that is biased and illuminated.

5.7. MKID Sensitivity

The number of quasiparticles in the MKID active volume exhibits fluctuations about the mean value N_{qp} due to the inherent randomness of the generation and recombination processes (116, 118); these fluctuations set the fundamental limit to sensitivity. In addition, non-fundamental effects such as amplifier noise and TLS noise must also be considered. We consider the case of an MKID that is illuminated by a steady stream of photons. The perturbation in the quasiparticle number $\delta N_{qp}(t)$ away from the mean value obeys the equation

$$\left(\frac{d}{dt} + \tau_{qp}^{-1}\right)\delta N_{qp}(t) = \frac{\eta_a\chi_{qp}}{\Delta_0}\delta P_a(t) + \frac{\eta_o}{\Delta_0}\delta P_o(t) + \delta\Gamma(t). \quad 75.$$

Here, $\eta_a = (\Delta_0/\chi_{qp})\partial\Gamma/\partial P_a$ is the differential efficiency with which readout power is converted to quasiparticles, $\delta P_a(t)$ represents a perturbation to the absorbed readout power, $\delta P_o(t)$ is the perturbation in the optical power, and $\delta\Gamma(t)$ represents the random shot noise due to quasiparticle generation and recombination. For simplicity, we assume that η_a is constant with P_a; the generalization to a power-dependent efficiency $\eta_a(P_a, P_o)$ is possible but does not fundamentally change the results. The shot noise has a white spectrum with an autocorrelation function that has the form

$$\langle\delta\Gamma(t)\delta\Gamma(t')\rangle = S_\Gamma\delta(t - t'), \quad 76.$$

where the spectral density is

$$S_\Gamma = \left(\frac{\eta_o h\nu}{\Delta_0}\right)^2\frac{P_o}{h\nu}(1 + n_o) + 2\frac{\eta_a\chi_{qp}}{\Delta_0}P_a + 2\Gamma_{th} + 2\Gamma_r \quad 77.$$

and is the sum of the noise arising from photon absorption, microwave quasiparticle generation, thermal quasiparticle generation, and recombination. The factor $(1 + n_o)$ accounts for photon bunching (119), where n_o is the photon occupation number, and the factors of two account for the fact that quasiparticles appear and disappear in pairs. The rates for the latter two processes are given by

$$\Gamma_{th} = \frac{N_{th}}{2}(\tau_{\max}^{-1} + \tau_{th}^{-1}) \quad 78.$$

and

$$\Gamma_r = \frac{N_{qp}}{2}(\tau_{\max}^{-1} + \tau_{qp}^{-1}), \tag{79.}$$

where $N_{th} = n_{th}V$ and τ_{th} is the lifetime if only thermal quasiparticles are present. In writing Equation 77, we have assumed that the generation rates are additive;

$$\Gamma = \Gamma_o + \Gamma_a = \eta_o P_o/\Delta_0 + \eta_a P_a/\Delta_0. \tag{80.}$$

A Fourier solution to Equation 75 yields

$$\frac{\delta N_{qp}(\nu)}{N_{qp}} = \frac{1}{1 + j2\pi\nu\tau_{qp}}\left[\eta_a\chi_{qp}\frac{\delta P_a(\nu)}{P_{qp}} + \eta_o\frac{\delta P_o(\nu)}{P_{qp}} + \frac{\tau_{qp}S_\Gamma^{1/2}}{N_{qp}}\delta z(\nu)\right], \tag{81.}$$

where $P_{qp} = N_{qp}\Delta_0/\tau_{qp}$ and $\delta z(\nu)$ is unit-variance white noise, $\langle \delta z(\nu)\delta z^*(\nu')\rangle = \delta(\nu - \nu')$. The perturbation in the absorbed readout power $\delta P_a(\nu)$ is the result of changes in the resonator frequency and dissipation, and is given by

$$\delta P_a(\nu) = P_g Q_i\Big\{F_x(\nu)\big[\delta x(\nu) + \delta x_{\rm TLS}(\nu)\big] + F_D(\nu)\delta Q_i^{-1}(\nu)\Big\}, \tag{82.}$$

where the response function for frequency perturbations is

$$F_x(\nu) = \chi_a\frac{2Q_c}{Q_i + Q_c}\frac{2Q_r x}{1 + 4Q_r^2x^2}\,\zeta(\nu,\omega)\zeta^*(-\nu,\omega), \tag{83.}$$

whereas the response function for dissipation perturbations is

$$F_D(\nu) = \chi_a\left[\frac{Q_i - Q_c}{Q_i + Q_c} + \frac{2Q_c}{Q_i + Q_c}\frac{4Q_r^2x^2}{1 + 4Q_r^2x^2}\,\zeta(\nu,\omega)\zeta^*(-\nu,\omega)(1 + j2Q_r\nu/\nu_r)\right]. \tag{84.}$$

Note that F_x and the frequency-dependent portion of F_D both vanish for zero detuning $x = 0$, and that the remaining term in F_D vanishes for optimum coupling $Q_c = Q_i$. These feedback effects could be carried through the analysis without difficulty, but from now on we drop them for simplicity.

At signal frequencies that are high enough so that the quasiparticle lifetime and resonator ring-down time may not be neglected, Equations 81 and 73 show that the frequency and dissipation perturbations may no longer result in motions δS_{21} that are purely tangent or normal to the resonance circle. Nonetheless, it is still possible to find suitable estimators to convert the measured transmission perturbations $\delta S_{21}(t)$ into values for the frequency and dissipation perturbations $\delta x(t)$ and $\delta Q_i^{-1}(t)$. To avoid this complication, we work in the adiabatic limit and with zero detuning. In this limit, examination of Equations 73 and 81 shows that we may define a dissipation estimator that converts motions normal to the resonance circle into estimates for the changes in optical power:

$$\begin{aligned}\delta\hat{P}_o^{(\rm diss)}(\nu) &= \frac{4P_{qp}}{\eta_o\chi_c\chi_{qp}}{\rm Re}\delta S_{21}(\nu)\\ &= \delta P_o(\nu) + \frac{\Delta_0}{\eta_0}S_\Gamma^{1/2}\delta z(\nu) + \frac{4P_{qp}}{\eta_o\chi_c\chi_{qp}}\delta S_a(\nu).\end{aligned} \tag{85.}$$

The noise-equivalent power (NEP) for dissipation readout is obtained by calculating the spectral density of the fluctuation terms:

$$\mathrm{NEP}^2_{\mathrm{diss}} = 2P_o h\nu(1+n_o) + \frac{8N^2_{qp}\Delta_0^2}{\eta_o^2\chi_c\chi_{qp}^2\tau_{qp}^2}\frac{kT_a}{P_a} + \frac{4\eta_a\chi_{qp}\Delta_0}{\eta_o^2}P_a + \frac{4\Gamma_{th}\Delta_0^2}{\eta_o^2} + \frac{2N_{qp}\Delta_0^2}{\eta_o^2}(\tau_{\max}^{-1}+\tau_{qp}^{-1}). \quad 86.$$

The terms in this equation are due to photon noise, amplifier noise, and shot noise from microwave generation of quasiparticles, thermal generation, and quasiparticle recombination, respectively. The factor of two arises from contributions from both positive and negative frequencies. Meanwhile, for frequency readout we would use the estimator,

$$\delta\hat{P}_o^{(\mathrm{freq})}(\nu) = \frac{4P_{qp}}{\beta\eta_o\chi_c\chi_{qp}}\mathrm{Im}\delta S_{21}(\nu), \quad 87.$$

which would lead to a noise equivalent power of

$$\mathrm{NEP}^2_{\mathrm{freq}} = 2P_o h\nu(1+n_o) + \mathrm{NEP}^2_{\mathrm{g-r}} + \frac{8N^2_{qp}\Delta_0^2}{\beta^2\eta_o^2\chi_c\chi_{qp}^2\tau_{qp}^2}\frac{kT_a}{P_a} + \frac{8N^2_{qp}\Delta_0^2Q_i^2}{\beta^2\eta_o^2\chi_{qp}^2\tau_{qp}^2}S_{\mathrm{TLS}}. \quad 88.$$

The photon noise and generation-recombination noise terms are unchanged, but the amplifier noise picks up a factor $1/\beta^2$. Also, the TLS noise must now be included, characterized here by the spectral density S_{TLS} for the fractional frequency shift. The response roll-off due to the quasiparticle lifetime may be accounted for by multiplying the amplifier and TLS contributions by a factor $1+(2\pi\nu\tau_{qp})^2$; the amplifier noise receives an additional factor of $1+(2Q_r\nu/\nu_r)^2$ due to the finite resonator bandwidth.

These expressions may be simplified somewhat by writing

$$\frac{N_{qp}}{\tau_{qp}} = \Gamma g(x), \quad 89.$$

where $x = \Gamma\tau_{\max}/N^* \geq 0$ and

$$g(x) = \frac{2}{1+1/\sqrt{1+2x}}. \quad 90.$$

Note that $1 \leq g(x) \leq 2$. If we define $y_a = \Gamma_a/\Gamma_o = \eta_a P_a/\eta_o P_o$ to be the ratio of the microwave and optical quasiparticle generation rates and assume that the thermal generation rate is made negligibly small, we may write

$$\mathrm{NEP}^2_{\mathrm{diss}} = 2(1+n_o)P_o h\nu + \frac{8g^2(x)\eta_a}{\chi_c\chi_{qp}^2\eta_o}\frac{(1+y_a)^2}{y_a}P_o kT_a + \frac{4\chi_{qp}}{\eta_o}y_a P_o\Delta_0 + \frac{4}{\eta_o}(1+y_a)P_o\Delta_0. \quad 91.$$

Rearranging,

$$\mathrm{NEP}^2_{\mathrm{diss}} = 2(1+n_o)P_o h\nu + \left[\frac{2g^2(x)\eta_a}{\chi_c\chi_{qp}^2}\frac{kT_a}{\Delta_0}\frac{(1+y_a)^2}{y_a} + (\chi_{qp}+1)y_a + 1\right]\frac{4P_o\Delta_0}{\eta_o}. \quad 92.$$

The factor in the square brackets is labeled $\mathcal{F}$, and is minimized when the readout power obeys

$$y_a = y_{\min} = \frac{1}{\sqrt{1 + (\chi_{qp} + 1)\chi_c \chi_{qp}^2 \Delta_0 / 2g^2(x)\eta_a kT_a}} < 1, \qquad 93.$$

so the microwave quasiparticle generation rate may approach but should not exceed the optical generation rate. The minimum value for $\mathcal{F}$ is

$$\mathcal{F} = \frac{4g^2(x)\eta_a}{\chi_c \chi_{qp}^2} \frac{kT_a}{\Delta_0} \left(1 + \frac{1}{y_{\min}}\right) + 1. \qquad 94.$$

In performing this minimization, we have neglected the variation of $g(x)$ with y_a. This is legitimate because $g(x)$ varies only rather slowly with x; in fact, $\partial \ln g / \partial \ln x \leq 1/8$. We therefore arrive at the following result:

$$\mathrm{NEP}_{\mathrm{diss}}^2 = \left[(1 + n_o)h\nu + \frac{8g^2(x)\eta_a}{\chi_c \chi_{qp}^2 \eta_o} \left(1 + \frac{1}{y_{\min}}\right) kT_a + \frac{2\Delta_0}{\eta_o}\right] 2P_o. \qquad 95.$$

Comparison of the first two terms in this equation leads to the necessary condition

$$kT_a < \frac{1 + n_0}{16g^2(x)} h\nu \qquad 96.$$

in order for the photon noise to dominate the amplifier noise. Assuming conservatively that $\eta_a \approx \eta_o$, ground-based submillimeter astronomy at $\lambda = 350$ μm requires $T_a < 5$ K, a value that is demanding but achievable with cooled microwave amplifiers using high electron mobility field-effect transistors (HEMT) or silicon-germanium bipolar transistors. In fact, photon noise–limited operation has now been reported for a detector operating at $\lambda = 0.9$ mm (120). For this experiment, the absorbed microwave power was comparable to or larger than the optical power, indicating that $\eta_a < \eta_o$. The third term in Equation 95 representing recombination noise becomes important when operating close to the gap frequency $\nu_g = 2\Delta/h$ (note $\eta_o \to 1$ in this case), and then only if photon bunching is not large, $n_o < 1$.

A similar analysis may be worked out for the case of frequency readout, starting with rewriting Equation 88 as

$$\begin{aligned} \mathrm{NEP}_{\mathrm{freq}}^2 = {} & 2(1 + n_o)P_o h\nu + 2\left(\frac{4N_0\Delta_0^2 V}{\alpha\gamma\eta_o S_2(\omega)\tau_{qp}}\right)^2 S_{\mathrm{TLS}} \\ & + \left[\frac{2g^2(x)\eta_a}{\chi_c \chi_{qp}^2 \beta^2} \frac{kT_a}{\Delta_0} \frac{(1 + y_a)^2}{y_a} + (\chi_{qp} + 1)y_a + 1\right] \frac{4P_o\Delta_0}{\eta_o}, \end{aligned} \qquad 97.$$

where we have used Equations 70, 72, and 74 to express the TLS noise term. The use of frequency readout considerably relaxes the requirements on the amplifier noise because $\beta^2(\omega) >> 1$ (see **Figure 18**), so other noise terms will dominate, particularly the TLS noise. Equation 97 shows that a large kinetic inductance fraction, long quasiparticle lifetime, small volume, and small gap energy are important for achieving a low TLS NEP. At low illumination levels ($\Gamma\tau_{\max} << N^*$), the quasiparticle lifetime reaches its maximum value $\tau_{\max}$; and because experimentally it is observed that $\tau_{\max} \sim \Delta_o^{-2}$, the TLS-limited dark NEP may be expected to

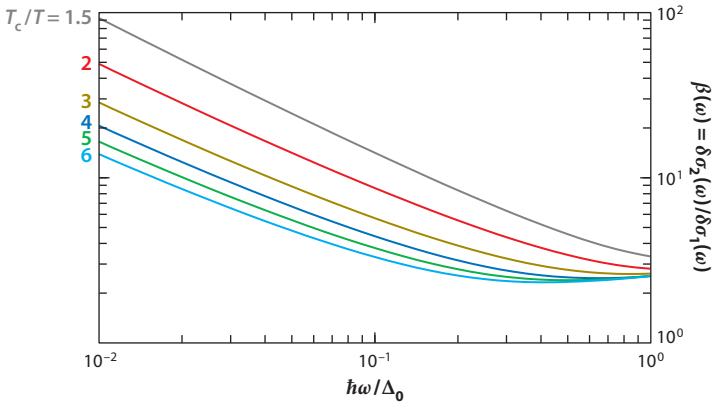

Figure 18

This figure shows the ratio $\beta(\omega)$ of the reactive ($\delta\sigma_2$) and dissipative ($\delta\sigma_1$) perturbations to the conductivity that result from a perturbation in the quasiparticle density (see Equation 74). A thermal quasiparticle distribution $f(E)$ is assumed. The increase of β with increasing temperature and decreasing frequency can be understood by examining the response functions $K_1(E)$ and $K_2(E)$ shown in **Figure 16**; K_1 has a negative peak near $E = \Delta_0 + \hbar\omega$ due to the downward transition to states near the gap $E = \Delta_0$. This stimulated emission process reduces the net absorption of power from the microwave field.

improve very rapidly as T_c is reduced, $\mathrm{NEP_{TLS}} \sim T_c^{-4}$. Meanwhile, at high illumination levels we calculate $\tau_{qp} \approx \sqrt{\tau_{\max}\Delta_0 n^*/2\eta_o P_o}$, and

$$\mathrm{NEP_{TLS}} = \frac{8N_0\Delta_0 V}{\alpha\gamma S_2(\omega)}\sqrt{\frac{S_{\mathrm{TLS}}}{\tau_{\max} n^* V\eta_o}}\sqrt{P_o\Delta_o}\,. \qquad 98.$$

The first two factors are dimensionless, and their product must be of order unity if the TLS noise is to be comparable to the recombination noise. Note that the product,

$$n^*\tau_{\max} = \tau_0(4N_0\Delta)(2\Delta_0/kT_c), \qquad 99.$$

may be expressed using the electron-phonon time constant τ_0 defined and tabulated by Kaplan et al. (121). Defining $F = 2\Delta_0/kT_c \approx 3.5$, we have

$$\mathrm{NEP_{TLS}} = \frac{4}{\gamma S_2(\omega)\sqrt{F}}\sqrt{\frac{N_0\Delta_0 V S_{\mathrm{TLS}}}{\alpha^2\tau_0\eta_o}}\sqrt{P_o\Delta_0}\,. \qquad 100.$$

The first factor is near unity; the TLS noise therefore becomes comparable to the recombination noise when $S_{\mathrm{TLS}} \approx \alpha^2\tau_0/N_0\Delta_0 V$. For $V = 1{,}000\ \mu\mathrm{m}^3$, the numerical values work out to be $S_{\mathrm{TLS}} \sim \alpha^2 \times 10^{-21}\ \mathrm{Hz}^{-1}$ for niobium and $S_{\mathrm{TLS}} \sim \alpha^2 \times 10^{-16}\ \mathrm{Hz}^{-1}$ for aluminum; these values may be compared with the experimental values given in Section 5.4.

5.8. Engineering Estimates for Two-Level System Noise

For practical design of detector arrays, it is often necessary to maintain the resonator quality factor Q_r above some minimum value that is set by the desired density of frequency multiplexing. In this case, it is useful to combine Equations 88 and 89 to obtain an expression for the TLS noise that sets the threshold for photon noise–limited operation:

$$S_{\mathrm{TLS}} < \frac{\beta^2}{4Q_{qp}^2}\frac{1+n_o}{n_o\Delta\nu}\frac{1}{(1+y_a)^2 g^2(x)}\,.$$

Here $\Delta\nu = P_o/n_o h\nu$ is the effective optical bandwidth. It is interesting to note that this condition is far easier to meet for spectroscopy (small $\Delta\nu$) than for imaging (large $\Delta\nu$). For concreteness, we examine the case of ground-based imaging at submillimeter wavelengths. We stipulate that $Q_{qp} \approx 2 \times 10^5$ is needed for good multiplexing, $n_o \sim 1$ at the detector, and $\Delta\nu \sim 100$ GHz for the 350 μm or 450 μm atmospheric windows. It is safe to assume that $(1 + y_a)\, g(x) \leq 2$. Also, at microwave frequencies (few GHz), $\beta \sim 4$. Therefore,

$$S_{\mathrm{TLS}} < \frac{16}{16 \times 10^{10}} \times \frac{2}{10^{11}\mathrm{Hz}} \times \frac{1}{4} = 5 \times 10^{-22}\mathrm{Hz}^{-1}.$$

Inspection of **Figure 14** illustrates the difficulty of reaching this level of performance. There are at least four solutions available: (*a*) Sacrifice multiplexing by reducing Q_{qp}; (*b*) increase the capacitor area; (*c*) use dissipation readout instead; or (*d*) reduce the readout frequency, taking advantage of the $\beta \propto 1/\omega_r$ dependence.

5.9. MKID Examples

One of the key issues for MKID design is the method used to couple the photons to be detected into the resonator. Early experiments avoided this issue by flood-illuminating the entire chip with X-rays and measuring the pulse response. Later, more sophisticated versions used a Ta strip as the X-ray absorber with two Al MKIDs at opposite ends of the strip (122), making use of quasiparticle diffusion and trapping. **Figure 19** shows the first attempt to achieve efficient coupling in the millimeter-wave band by using slot-array antennas feeding CPW MKID resonators (105, 123, 124). In later versions of these devices, the capacitive portion of the CPW resonator has been replaced by an interdigitated capacitor in order to reduce the noise (100). A multiband millimeter-wave astronomical camera using this array design is now being prepared for use on the Caltech Submillimeter Observatory (125). As another example, Yates et al. (120) used a hemispherical lens and a twin-slot antenna to feed a CPW MKID.

A much simpler and very clever solution to this problem was the lumped-element resonator suggested by Doyle et al. (62) and shown in **Figure 1**, in which the inductor simultaneously serves as the radiation absorber. Another design along these lines, except using a microstrip resonator, was described by Brown et al. (126). Efficient radiation absorption requires either using very thin films of ordinary superconductors or using highly resistive superconductors such as TiN; a very convenient feature of using TiN films is that T_c may be easily adjusted by changing the stoichiometry (61). Designing for high-absorption efficiency simultaneously guarantees a high kinetic inductance fraction α; this can be understood through the Mattis-Bardeen relation between the surface inductance and surface resistance, $L_s = \hbar R_s/\pi\Delta_0$. The lumped-element pixel design is being used for the $\lambda = 2$-mm band in the NIKA camera built for the IRAM 30-m telescope (127).

Microwave cross talk is a serious problem with this design; however, it is possible to produce large arrays with negligible cross talk levels (128, 128a) by modifying the inductor design using opposite-polarity conductor pairs in close proximity to minimize the microwave dipole moment (see **Figure 20**). In addition, efficient dual-polarization absorption may be obtained using appropriate metallization patterns. A variety of lumped-element, TiN-based MKIDs are now being developed for a wide range of applications including photon detection at millimeter, submillimeter, far-IR, UV/optical (129), and X-ray wavelengths as well as dark matter detection.

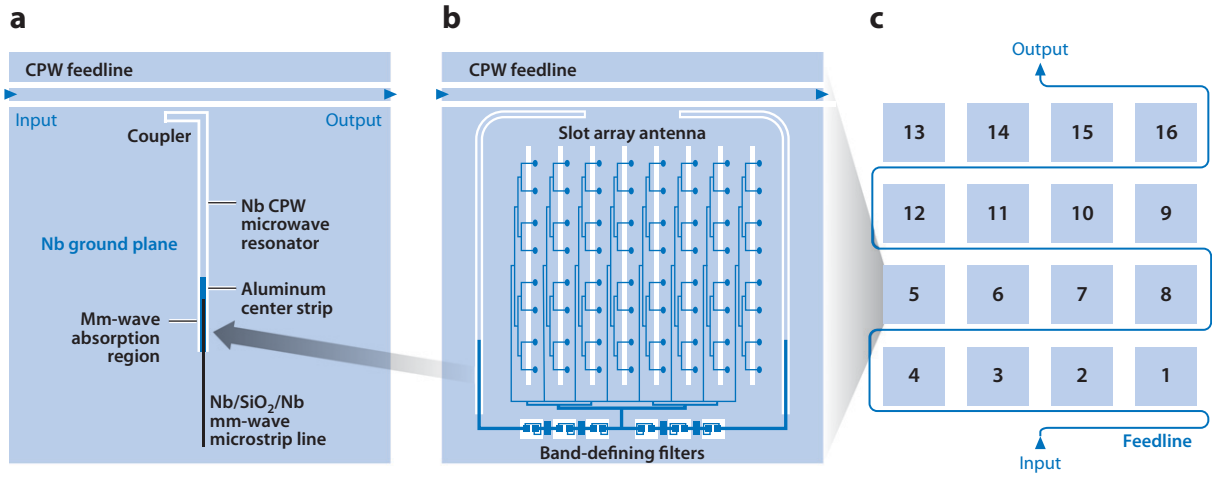

Figure 19

This figure illustrates the antenna-coupled microwave kinetic inductance detector (MKID) arrays developed at Caltech/JPL. (*a*) A $\lambda/4$ coplanar-waveguide (CPW) resonator is coupled to a CPW feedline. Millimeter-wave radiation is brought to the resonator using a niobium microstrip line and is absorbed by the aluminum section of the CPW resonator's center strip. (*b*) A phased-array multislot antenna, two CPW MKIDs, and on-chip band-defining filters are used to make a dual-band pixel. (*c*) A 4 × 4 pixel array is multiplexed using a single feedline.

The ultimate sensitivity achievable with MKIDs is not yet known. Measurements of $T_c = 1.1$ K TiN CPW resonators (61) give values of NEP $\approx 4 \times 10^{-19}$ W Hz$^{-1/2}$ at $\nu = 1$ Hz for dissipation readout; comparable numbers have been obtained using the best Al CPW resonators (116, 130). However, the TiN result was achieved using a relatively low value of $Q_c \sim 5 \times 10^4$, so NEPs in the low 10^{-20} W Hz$^{-1/2}$ range should therefore be possible using higher-Q resonators. The corresponding energy sensitivity $\sigma_E = \text{NEP}\sqrt{\tau_{qp}}$ indicates that photon counting in the far-IR should be possible.

5.10. Superconducting Microresonator Bolometers

Given the considerable progress that has been made in the performance and physical understanding of microresonators, as well as the advances in digital frequency-multiplexed readout electronics, McDonald's kinetic inductance bolometer concept (89) is worth revisiting. Superconducting microresonators have been successfully fabricated on thermally suspended silicon nitride micromesh (H.G. Leduc & P.K. Day, personal communication), so a frequency-multiplexed array of bolometers is straightforward to produce. In a standard MKID, quasiparticle recombination provides the bottleneck for power flow, whereas in a bolometer, the bottleneck is set by the geometry of the thermal suspension legs. Therefore, the resonator-bolometer is an interesting option when quasiparticle recombination is too rapid, e.g., at higher temperatures. The thermally suspended island also provides an opportunity to spread the absorbed photon energy uniformly across the inductor, which maximizes responsivity. In contrast, this is often not easy to achieve in antenna-coupled MKIDs. In addition, the quasiparticle recombination noise may be greatly reduced. Importantly, the noise performance of available transistor amplifiers is considerably better than is needed to reach the fundamental sensitivity limits for bolometers (e.g., photon or phonon noise).

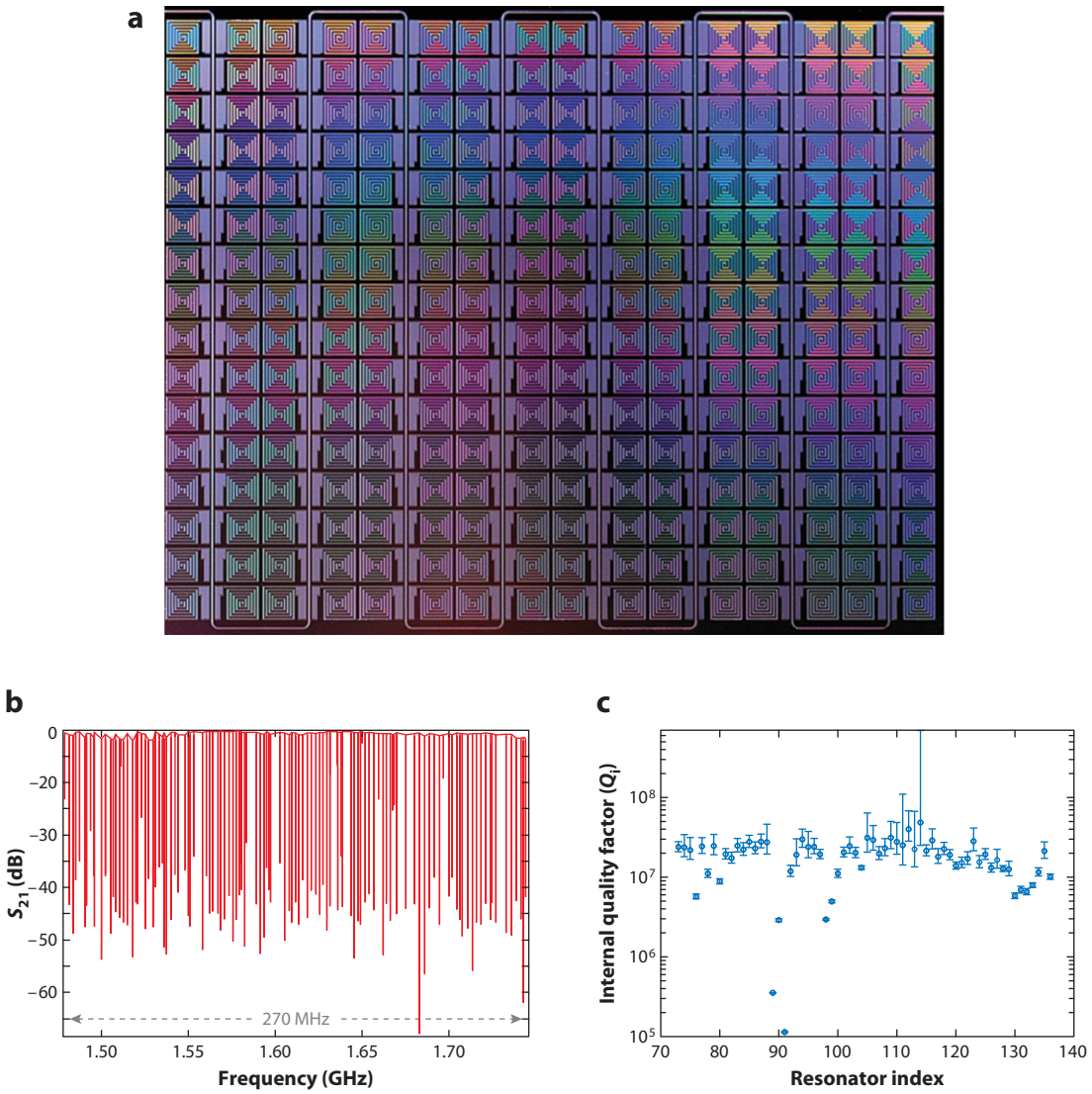

Figure 20

(*a*) A 16 × 16 array of TiN lumped-element microwave kinetic inductance detectors using a spiral inductor and an interdigitated capacitor. The pixels are approximately 0.6 mm in size. (*b*) The measured resonances for half the array (128 pixels) are very deep and fall into a 270-MHz band centered at 1.6 GHz. (*c*) The internal quality factors are very high, $Q_i > 10^7$, with good uniformity. Credit: O. Noroozian, P.K. Day, B.-H. Eom & H.G. Leduc.

6. OTHER APPLICATIONS

6.1. TES Bolometer Multiplexing

In a transition edge sensor (TES) bolometer (131), a superconducting strip operating on its resistive transition is used as a sensitive thermometer. The strip is biased by applying a voltage source rather than a current source; this arrangement provides the negative electrothermal feedback that is needed to stabilize the TES on its transition. The now-standard method for

readout of large arrays of TES bolometers involves time-domain multiplexing using SQUIDs (132). An alternative scheme making use of superconducting microresonators may offer higher multiplexing densities (133). In this scheme, the TES current is sent through a planar coil that couples flux into a single-junction SQUID that is coupled to a microresonator. A change in the TES current causes a change in the SQUID inductance and, therefore, the resonator frequency. In this way, a TES array can be read out using the same frequency-domain scheme as used for MKIDs. Through the addition of Josephson-junction current-steering switches, a code-division multiplexing scheme may be overlaid (134), further increasing the multiplexing density.

6.2. Parametric Amplifiers

As discussed in Section 5.5, superconductors have an intrinsic nonlinearity in which, to lowest order, the kinetic inductance varies quadratically with current. That reactive nonlinearities can be used for low-noise amplification has been known for at least a century; the use of the kinetic inductance nonlinearity for this purpose was suggested and patented by Landauer (50). Shortly thereafter, amplification was demonstrated using an ultrathin superconducting film coupled with a waveguide-fed rutile resonator (135); subsequent work (136) called into question whether the kinetic inductance or intergrain weak links provided the relevant nonlinearity. This is a key issue, because low-noise parametric amplification requires that the nonlinear reactance have low dissipation. The first clear-cut demonstration of parametric amplification using the kinetic inductance nonlinearity has been given only quite recently (51), using niobium CPW resonators similar to the one shown in **Figure 5**. An alternative approach is to use a series array of Josephson junctions or SQUIDs to provide the reactive nonlinearity for a resonator (137). One advantage of this technique is that the resonance frequency may be readily tuned through the application of a magnetic field. An interesting hybrid is to use nanobridges in place of tunnel junctions. The nanobridges essentially act as discrete kinetic inductors, and their small size allows the inductance nonlinearity to be accessed at a reduced current scale. Parametric amplifiers using this concept have recently been demonstrated (138).

6.3. Quantum Systems

In recent years, the most visible application of superconducting microresonators has been in experiments exploring the prospects for superconducting quantum computing. Superconducting microresonators are a key component for these experiments, and their dissipation must be kept very low in order to prevent loss of quantum coherence, so the use of CPW resonators has had a large impact. The first such experiment to incorporate CPW resonators was performed by the Schoelkopf group at Yale (2). In this experiment, a Cooper pair box (CPB) acting as a two-level atom was fabricated next to a CPW resonator. In essence, this is a circuit version of a single atom in an optical cavity. The use of a superconducting microresonator allowed the strong-coupling regime to be achieved, in which the vacuum Rabi frequency is considerably larger than the relaxation rates of the CPB and resonator. This circuit-QED experiment received considerable attention, and led to the adoption of superconducting microresonators in a number of other low-temperature experiments. One particularly interesting example is the use of superconducting microresonators to probe the motion of nanomechanical resonators into the quantum regime (139, 140). The possibility of using microresonators to measure the spin state of a single-molecule magnet has also been considered (141). Another intriguing spin-off of this work is the proposal to use superconducting microresonators to implement photon lattices, with a goal of providing a way to engineer

strongly correlated many-body systems (142, 143). This concept has the potential to open up a broad new area of research in many-body physics. We close this section by mentioning the clever experiment of Wilson et al. (144), in which a SQUID acting as a variable inductor was incorporated at the end of a CPW resonator structure. By driving the SQUID with a time-varying field so that its inductance is modulated, this system can be made to simulate an optical cavity in which one of the end mirrors oscillates back and forth at twice the frequency of the cavity resonance. The goal here is to demonstrate the dynamical Casimir effect: the spontaneous production of photons from the cavity vacuum. In fact, Wilson et al. do see radiation emanating from their CPW resonator, but as they explain, it is necessary to firmly establish that the cavity starts off in the ground state before claiming a demonstration of the dynamical Casimir effect.

FUTURE ISSUES

Over the past decade, interest in superconducting microresonators has expanded very rapidly as a result of the wide variety of applications at the forefront of research. Although considerable progress has been made in understanding the underlying physics of these devices, substantial work remains to be done in a number of areas. Here we reiterate the areas that need attention:

1. The advances in our understanding of the physical location of the TLS and their effect on resonator properties provide an opportunity to develop improved resonator designs and fabrication methods, with the goal of minimizing dissipation and noise. The crystalline silicon parallel-plate capacitor demonstrated by Weber et al. (81) is a first step in this direction.
2. Although a detailed microscopic model for the TLS-induced frequency shift and dissipation is available and quantitatively explains the experimental results, no corresponding model is available for the TLS noise. The $f^{-1/2}$ spectral shape is not understood, and the physics of the noise—whether it results from TLS-phonon interactions, or TLS-TLS interactions, or both—is not clear. Additional measurements covering a wider range of parameter space—frequency, temperature, power, materials, etc.—may shed additional light on this question.
3. Nearly five decades after the initial proposals, the intrinsic kinetic inductance nonlinearity of superconductors is finally being put to use in devices such as parametric amplifiers (51). The time is ripe for a more thorough exploration of the possible uses of this nonlinearity, as well as the investigation of this nonlinearity mechanism in a wider range of superconducting materials. The use of nanobridges as nonlinear inductive elements in quantum circuits is particularly interesting (138, 145).
4. Microresonator measurements have significantly improved our understanding of quasparticle dynamics, especially the quasiparticle lifetime. However, the physical mechanism that causes the lifetime to saturate at low temperatures is still not understood. Further studies of the lifetime, the influence of impurities, and especially the fluctuations of the quasiparticles (116) are needed. The use of ultralow noise superconducting parametric amplifiers, as illustrated by Gao et al. (99), will be of considerable help.
5. MKIDs are usually operated in a regime in which nonlinear effects are important. This includes both the intrinsic kinetic inductance nonlinearity and the additional

nonlinearity that results from quasiparticle heating and pair-breaking due to the absorption of microwave power. A detailed theory of these effects is needed, perhaps building on the Chang-Scalapino theory (21), validated by comparison to experiment.

6. The discovery that TiN (61) and other highly resistive superconductors can have exceptionally low microwave loss opens up broad new areas of investigation, especially for MKIDs, but also for other applications. Although TiN is well known for its excellent mechanical properties and has widespread room-temperature applications, considerable work remains to be done to investigate the superconducting properties of TiN films and how these correlate with other properties, e.g., the film microstructure (63). In addition, the electrodynamic response of these materials needs to be studied in detail and compared to the Mattis-Bardeen predictions, including the possibility of a broadening of the density of states (see Section 2.4).
7. The resonator bolometer—a hybrid between MKIDs and bolometers—is basically a microwave version of McDonald's (89) kinetic inductance bolometer concept. This structure is considerably simpler than the TES/SQUID bolometer and could provide a versatile solution for a number of detector applications.

DISCLOSURE STATEMENT

The author is not aware of any affiliations, memberships, funding, or financial holdings that might be perceived as affecting the objectivity of this review.

ACKNOWLEDGMENTS

It has been enormously enjoyable to watch this field develop over the past decade. I am particularly grateful to my JPL colleagues and collaborators, especially Rick Leduc and Peter Day, without whom nothing would have happened. I have learned a tremendous amount from my students and postdocs, past and present: Jiansong Gao, Shwetank Kumar, Ben Mazin, Chris McKenney, Tony Mrockowski, Omid Noroozian, Erik Shirokoff, Loren Swenson, and Tasos Vayonakis. I have benefitted greatly from stimulating and useful conversations with a number of scientists, including Rami Barends, Jochem Baselmans, Simon Doyle, Jason Glenn, Sunil Golwala, Kent Irwin, Teun Klapwijk, Konrad Lehnert, John Martinis, Phil Mauskopf, Harvey Moseley, Steve Padin, David Pappas, Dan Prober, Bernard Sadoulet, Rob Schoelkopf, and Stafford Withington. The Caltech/JPL devices mentioned here were fabricated at the JPL Microdevices Laboratory. JPL is operated by the California Institute of Technology, under a contract with the National Aeronautics and Space Administration. This work was supported in part by NASA grant NNX10AC83G, JPL, the Gordon and Betty Moore Foundation, and the Keck Institute for Space Studies.

LITERATURE CITED

1. Day PK, Leduc HG, Mazin BA, Vayonakis A, Zmuidzinas J. 2003. *Nature* 425:817–21
2. Wallraff A, Schuster DI, Blais A, Frunzio L, Huang RS, et al. 2004. *Nature* 431:162–67
3. Zmuidzinas J, Richards PL. 2004. *Proc. IEEE* 92:1597–616
4. Moseley SH. 2009. *AIP Conf. Proc.* 1185:9–19

5. Mazin BA. 2009. *AIP Conf. Proc.* 1185:135–43
6. Irwin KD, Hilton GC. 2005. *Top. Appl. Phys.* 99:63–149
7. Cabrera B, Miller A, Young B. 2009. *Proc. Int. Workshop Low Temp. Detect., 13th, Stanford*, 1185:20–24. Melville, NY: AIP
8. Kamerlingh Onnes H. 1911. *Commun. Phys. Lab. Univ. Leiden* 67:657–58
9. Silsbee FB, Scott RB, Cook JW, Brickwedde FG. 1932. *Phys. Rev.* 39:379–80
10. McLennan JC, Burton AC, Pitt A, Wilhelm JO. 1932. *Proc. R. Soc. A* 136:52–76
11. London H. 1940. *Proc. R. Soc. A* 176:522–33
12. Daunt JG, Keeley TC, Mendelssohn K. 1937. *Philos. Mag.* 23:264–71
13. Andrews DH, Brucksch WF, Ziegler WT, Blanchard ER. 1941. *Phys. Rev.* 59:1045–46
14. Blevins GS, Gordy W, Fairbank WM. 1955. *Phys. Rev.* 100:1215–16
15. Glover RE, Tinkham M. 1956. *Phys. Rev.* 104:844–45
16. Glover RE, Tinkham M. 1957. *Phys. Rev.* 108:243–56
17. Bardeen J, Cooper LN, Schrieffer JR. 1957. *Phys. Rev.* 106:162–64
18. Bardeen J, Cooper LN, Schrieffer JR. 1957. *Phys. Rev.* 108:1175–204
19. London H. 1934. *Nature* 133:497–98
20. Mattis DC, Bardeen J. 1958. *Phys. Rev.* 111:412–17
21. Chang JJ, Scalapino DJ. 1977. *Phys. Rev. B* 15:2561–670
22. Turneaure JP, Halbritter J, Schwettman HA. 1991. *J. Supercond.* 4:341–55
23. Walsh PJ, Tomaselli VP. 1990. *Am. J. Phys.* 58:644–50
24. Gao J. 2008. *The physics of superconducting microwave resonators*. PhD thesis. Calif. Inst. Technol., Pasadena. 180 pp. **http://thesis.library.caltech.edu/2530**
25. Gao J, Zmuidzinas J, Vayonakis A, Day P, Leduc H. 2008. *J. Low Temp. Phys.* 151:557–63
26. Dynes RC, Garno JP, Hertel GB, Orlando TP. 1984. *Phys. Rev. Lett.* 53:2437–40
27. Barends R, Hortensius HL, Zijlstra T, Baselmans JJA, Yates SJC, et al. 2008. *Appl. Phys. Lett.* 92:223502
28. Noguchi, T, Naruse, M, Sekimoto, Y. 2011. *Phys. Procedia*. In press
29. Mitrović B, Rozema LA. 2008. *J. Phys. Condens. Matter* 20:015215
30. Larkin AI, Ovchinnikov YN. 1971. *Sov. Phys. JETP* 34:1144–50
31. Pekola JP, Maisi VF, Kafanov S, Chekurov N, Kemppinen A, et al. 2010. *Phys. Rev. Lett.* 105:026803
32. Bitter F, Garrison JB, Halpern J, Maxwell E, Slater JC, Squire CF. 1946. *Phys. Rev.* 70:97–98
33. Pippard AB. 1947. *Proc. R. Soc. A* 191:370–84; Pippard AB. 1947. *Proc. R. Soc. A* 191:399–415
34. Fairbank WM. 1949. *Phys. Rev.* 76:1106–11
35. Turneaure JP, Weissman I. 1968. *J. Appl. Phys.* 39:4417–27
36. Hartwig WH. 1973. *Proc. IEEE* 61:58–70
37. Septier A, Viet NT. 1977. *J. Phys. E: Sci. Instrum.* 10:1193–1207
38. Halbritter J. 1987. *Appl. Phys. A Mater. Sci. Process.* 43:1–28
39. Brattke S, Varcoe BTH, Walter H. 2001. *Phys. Rev. Lett.* 86:3534–37
40. Ciovati G. 2004. *J. Appl. Phys.* 96:1591–600
41. Ciovati G, Myneni G, Stevie F, Maheshwari P, Griffis D. 2010. *Phys. Rev. Spec. Top. Accel. Beams* 13:022002
42. Swihart JC. 1961. *J. Appl. Phys.* 32:461–69
43. Mason PV, Gould RW. 1969. *J. Appl. Phys.* 40:2039
44. Kautz RL. 1978. *J. Appl. Phys.* 49:308–14
45. Pond JM, Claasen JH, Carter WL. 1987. *IEEE Trans. Magn.* 23:903–6
46. Chang WH. 1979. *J. Appl. Phys.* 50:8129–34
47. Yassin G, Withington S. 1995. *J. Phys. D* 28:1983–91
48. Booth JC, Holloway CL. 1999. *IEEE Trans. Microw. Theory Tech.* 47:769–73
49. Gao J, Zmuidzinas J, Mazin BA, Day PK, Leduc HG. 2006. *Nucl. Instrum. Methods A* 559:585–87
50. Landauer RW. 1963. Superconductive parametric amplifier. *U. S. Patent No. 3,111,628*
51. Tholen EA, Ergul A, Doherty EM, Weber FM, Gregis F, Haviland DB. 2007. *Appl. Phys. Lett.* 90:253509

52. Barends R, Wenner J, Lenander M, Chen Y, Bialczak RC, et al. 2011. *Appl. Phys. Lett.* 99:113507
53. DiNardo AJ, Smith JG, Arams FR. 1971. *J. Appl. Phys.* 42:186–89
54. Pöpel R. 1983. *IEEE Trans. Microw. Theory Tech.* 31:600–4
55. Andreone A, DiChiara A, Peluso G, Santoro M, Attanasio C, et al. 1993. *J. Appl. Phys.* 73:4500
56. Martinis JM, Cooper KB, McDermott R, Steffen M, Ansmann M, et al. 2005. *Phys. Rev. Lett.* 95:210503
57. Mazin BA, Sank D, McHugh S, Lucero EA, Merrill A, et al. 2010. *Appl. Phys. Lett.* 96:102504
58. Mazin BA, Day PK, Zmuidzinas J, Leduc HG. 2002. *AIP Conf. Proc.* 605:309–12
59. Wisbey DS, Gao JS, Vissers MR, da Silva FCS, Kline JS, et al. 2010. *J. Appl. Phys.* 108:093918
60. Sage JM, Bolkhovsky V, Oliver WD, Turek B, Welander PB. 2011. *J. Appl. Phys.* 109:063915
61. Leduc HG, Bumble B, Day PK, Eom BH, Gao J, et al. 2010. *Appl. Phys. Lett.* 97:102509
62. Doyle S, Mauskopf P, Naylon J, Porch A, Dunscombe C. 2008. *J. Low Temp. Phys.* 151:530–36
63. Vissers MR, Gao J, Wisbey DS, Hite DA, Tsuei CC, et al. 2010. *Appl. Phys. Lett.* 97:232509
64. Meschke M, Guichard W, Pekola JP. 2006. *Nature* 444:187–190
65. Kominami M, Pozar DM, Schaubert DH. 1985. *IEEE Trans. Antenn. Propag.* 33:600–7
66. Zmuidzinas J, Leduc HG. 1992. *IEEE Trans. Microw. Theory Tech.* 40:1797–1804
67. Mazin B. 2003. *Microwave kinetic inductance detectors*. PhD thesis. Calif. Inst. Technol., Pasadena. 179 pp. **http://thesis.library.caltech.edu/3910**
68. Anderson PW, Halperin BI, Varma CM. 1972. *Philos. Mag.* 25:1–9
69. Phillips WA. 1972. *J. Low Temp. Phys.* 7:351–60
70. Jankowiak R, Small GJ, Ries B. 1987. *Chem. Phys.* 118:223–31
71. Phillips WA. 1987. *Rep. Prog. Phys.* 50:1657–1708
72. Gao J, Daal M, Vayonakis A, Kumar S, Zmuidzinas J, et al. 2008. *Appl. Phys. Lett.* 92:152505
73. Kumar S, Gao J, Zmuidzinas J, Mazin BA, Leduc HG, Day PK. 2008. *Appl. Phys. Lett.* 92:123503
74. Pappas DP, Vissers MR, Wisbey DS, Kline JS, Gao J. 2011. *IEEE Trans. Appl. Supercond.* 21:871–74
75. Frossati G, Gilchrist J, Lasjaunias JC, Meyer W. 1977. *J. Phys. Chem.* 10:L515–19
76. Von Schickfus M, Hunklinger S. 1977. *Phys. Lett.* 64A:144–46
77. O'Connell AD, Ansmann M, Bialczak RC, Hofheinz M, Katz N, et al. 2008. *Appl. Phys. Lett.* 92:112903
78. Paik H, Osborn KD. 2010. *Appl. Phys. Lett.* 96:072505
79. Gao JS, Zmuidzinas J, Mazin BA, Leduc HG, Day PK. 2007. *Appl. Phys. Lett.* 90:102507
80. Barends R, Vercruyssen N, Endo A, de Visser PJ, Zijlstra T, et al. 2010. *Appl. Phys. Lett.* 97:023508
81. Weber S, Murch KW, Slichter DH, Vijay R, Siddiqi I. 2011. *Appl. Phys. Lett.* 98:172510
82. Kim Z, Suri B, Zaretskey V, Novikov S, Osborn KD, et al. 2011. *Phys. Rev. Lett.* 106:120501
83. Mazin BA, Day PK, Irwin KD, Reintsema CD, Zmuidzinas J. 2006. *Nucl. Instrum. Methods A* 559:799–801
84. Yates SJC, Baryshev AM, Baselmans JJA, Klein B, Güsten R. 2009. *Appl. Phys. Lett.* 95:042504
85. Duan R, McHugh S, Serfass B, Mazin BA, Merrill A, et al. 2010. *Proc. SPIE* 7741:77411V
86. Richards PL. 1994. *J. Appl. Phys.* 76:1–24
87. Burstein E, Langenberg DN, Taylor BN. 1961. *Phys. Rev. Lett.* 6:92–94
88. Peacock A, Verhoeve P, Rando N, van Dordrecht A, Taylor BG. 1996. *Nature* 381:135–37
89. McDonald DG. 1987. *Appl. Phys. Lett.* 50:775–77
90. Bluzer N. 1995. *J. Appl. Phys.* 78:7340–51
91. Sergeev AV, Reizer MY. 1996. *Int. J. Mod. Phys. B* 10:635–67
92. Gulian AM, Van Vechten D. 1995. *Appl. Phys. Lett.* 67:2560–62
93. Van Vechten D, Porter FS, Wood KS, Gulian AM. 1996. *Nucl. Instrum. Methods A* 370:34–37
94. Jack MD. 1990. Frequency domain integrating resonant superconducting transmission line detector. *U.S. Patent No. 4,962,316*
95. Schoelkopf RJ, Moseley SH, Stahle CM, Wahlgren P, Delsing P. 1999. *IEEE Trans. Appl. Supercond.* 9:2935–39
96. Stevenson TR, Pellerano FA, Stahle CM, Aidala K, Schoelkopf RJ. 2002. *Appl. Phys. Lett.* 80:3012–14

97. Yoon J, Clarke J, Gildemeister JM, Lee AT, Myers MJ, et al. 2001. *Appl. Phys. Lett.* 78:371–73
98. Gao J, Daal M, Martinis JM, Vayonakis A, Zmuidzinas J, et al. 2008. *Appl. Phys. Lett.* 92:212504
99. Gao J, Vale LR, Mates JAB, Schmidt DR, Hilton GC, et al. 2011. *Appl. Phys. Lett.* 98:232508
100. Noroozian O, Gao J, Zmuidzinas J, Leduc HG, Mazin BA. 2009. *AIP Conf. Proc.* 1185:148–51
101. Barends R, Vercruyssen N, Endo A, de Visser PJ, Zijlstra T, et al. 2010. *Appl. Phys. Lett.* 97:033507
102. Pippard AB. 1950. *Proc. R. Soc. A* 203:210–23
103. Pippard AB. 1953. *Proc. R. Soc. A* 216:547–68
104. Healey JE, Lindstrom T, Colclough MS, Muirhead CM, Tzalenchuk AY. 2008. *Appl. Phys. Lett.* 93:043513
105. Schaerth J, Vayonakis A, Day P, Glenn J, Gao J, et al. 2008. *J. Low Temp. Phys.* 151:684–89
106. Parmenter RH. 1962. *RCA Rev.* 23:323–52
107. Anthore A, Pothier H, Esteve D. 2003. *Phys. Rev. Lett.* 90:127001
108. Romijn J, Klapwijk TM, Renne MJ, Mooij JE. 1982. *Phys. Rev. B* 26:3648–55
108a. Annunziata AJ, Santavicca DF, Frunzio L, Catelani G, Rooks MJ, et al. 2010. *Nanotechnology* 21:445202
109. Connell RA. 1963. *Proc. IEEE* 51:616–17
110. Golosovsky MA, Snortland HJ, Beasley MR. 1995. *Phys. Rev. B* 51:6462
111. Abdo B, Segev E, Shtempluck O, Buks E. 2006. *Phys. Rev. B* 73:134513
112. de Visser PJ, Withington S, Goldie DJ. 2010. *J. Appl. Phys.* 108:114504
113. Rothwarf A, Taylor BN. 1967. *Phys. Rev. Lett.* 19:27–30
114. Barends R, Baselmans JJA, Yates SJC, Gao JR, Hovenier JN, Klapwijk TM. 2008. *Phys. Rev. Lett.* 100:257002
115. Barends R, van Vliet S, Baselmans JJA, Yates SJC, Gao JR, Klapwijk TM. 2009. *Phys. Rev. B* 79:020509
116. de Visser PJ, Baselmans JJA, Diener P, Yates SJC, Endo A, Klapwijk TM. 2011. *Phys. Rev. Lett.* 106:167004
117. Kozorezov AG, Golubov AA, Wigmore JK, Martin D, Verhoeve P, et al. 2008. *Phys. Rev. B* 78:174501
118. Wilson CM, Frunzio L, Prober DE. 2001. *Phys. Rev. Lett.* 87:067004
119. Zmuidzinas J. 2003. *Appl. Opt.* 42:4989–5008
120. Yates SJC, Baselmans JJA, Endo A, Janssen RMJ, Ferrari L, et al. 2011. *Appl. Phys. Lett.* 99:07350
121. Kaplan SB, Chi CC, Langenberg DN, Chang JJ, Jafarey S, Scalapino DJ. 1976. *Phys. Rev. B* 14:4854–73
122. Mazin BA, Bumble B, Day PK, Eckart ME, Golwala S, et al. 2006. *Appl. Phys. Lett.* 89:222507
123. Kumar S. 2008. *Submillimeter wave camera using a novel photon detector technology.* PhD thesis. Calif. Inst. Technol., Pasadena. 132 pp. **http://thesis.library.caltech.edu/1663**
124. Schlaerth J. 2010. *Microwave kinetic inductance detector camera development for millimeter-wave astrophysics*. PhD. thesis, Univ. Colo., Boulder, CO
125. Maloney PR, Czakon NG, Day PK, Downes TP, Duan R, et al. 2010. *Proc. SPIE* 7741:77410F
126. Brown A-D, Hsieh W-T, Moseley SH, Stevenson TR. 2010. *Proc. SPIE* 7741:77410P
127. Monfardini A, Benoit A, Bideaud A, Swenson LJ, Roesch M. 2011. *Astrophys. J. Suppl. Ser.* 194:24
128. Noroozian O. 2012. *Superconducting microwave resonator arrays for submillimeter/far-infrared imaging* PhD thesis. Calif. Inst. Tech, Pasadena. In press
128a. Noroozian O, Day PK, Eom BH, Leduc HG, Zmuidzinas J. 2012. Crosstalk reduction for superconducting microwave resonator arrays. *IEEE Trans. Microw. Theory Tech*. In press
129. Mazin BA, O'Brien K, McHugh S, Bumble B, Moore D, et al. 2010. *Proc. SPIE* 7735:773518
130. Ferrari L, Baryshev AM, Baselmans JJA, de Lange G, Diener P, et al. 2010. *Proc. SPIE* 7731:77314H
131. Irwin KD. 1995. *Appl. Phys. Lett.* 66:1998–2000
132. Chervenak JA, Irwin KD, Grossman EN, Martinis JM, Reintsema CD, Huber ME. 1999. *Appl. Phys. Lett.* 74:4043–45
133. Mates JAB, Hilton GC, Irwin KD, Vale LR, Lehnert KW. 2008. *Appl. Phys. Lett.* 92:023514
134. Niemack MD, Beyer J, Cho HM, Doriese WB, Hilton GC, et al. 2010. *Appl. Phys. Lett.* 96:163509

135. Clorfeine AS. 1964. *Proc. IEEE* 52:844–45
136. Zimmer H. 1967. *Appl. Phys. Lett.* 10:193–95
137. Castellanos-Beltran MA, Irwin KD, Hilton GC, Vale LR, Lehnert KW. 2008. *Nat. Phys.* 4:929–31
138. Levenson-Falk EM, Vijay R, Siddiqi I. 2011. *Appl. Phys. Lett.* 98:123115
139. Teufel JD, Donner T, Castellanos-Beltran MA, Harlow JW, Lehnert KW. 2009. *Nat. Nanotechnol.* 4:820–23
140. Hertzberg JB, Rocheleau T, Ndukum T, Savva M, Clerk AA, Schwab KC. 2010. *Nat. Phys.* 6:213–17
141. Fan T, Tsifrinovich VI, Kent AD. 2011. *Phys. Rev. B* 84:024410
142. Greentree AD, Tahan C, Cole JH, Hollenberg LCL. 2006. *Nat. Phys.* 2:856–61
143. Koch J, Houck AA, Le Hur K, Girvin SM. 2010. *Phys. Rev. A* 82:043811
144. Wilson CM, Duty T, Sandberg M, Persson F, Shumeiko V, Delsing P. 2010. *Phys. Rev. Lett.* 105:233907
145. Ku J, Manucharyan V, Bezryadin A. 2010. *Phys. Rev. B* 82:134518

Annual Review of Condensed Matter Physics

Volume 3, 2012

Contents

Errata

An online log of corrections to *Annual Review of Condensed Matter Physics* articles may be found at http://conmatphys.annualreviews.org/errata.shtml